Energy, Exergy and Computing Efficiency Based Data Center Workload and Cooling Management

Rohit Gupta [1]*, Sahar Asgari* [1,3]*, Hosein Moazamigoodarzi* [3]*, Douglas G. Down* [2,3]**, Ishwar K. Puri* [1,3]

[1]Department of Mechanical Engineering, McMaster University, Hamilton, Ontario, Canada.

[2]Department of Computing and Software, McMaster University, Hamilton, Ontario, Canada.

[3]Computing Infrastructure Research Centre, McMaster University, Hamilton, Ontario, Canada.

AUTHOR INFORMATION

*Corresponding author

McMaster University

1280 Main St. W.

Hamilton, ON L8S 4L8, Canada

Email: downd@mcmaster.ca

Abstract

The rapidly rising computing workloads in data centers (DCs) have necessitated new approaches to ensure effective performance and resilience that minimize the associated cooling energy. The literature on thermally-aware workload management provides strategies to reduce this energy cost, while typically ignoring the reduction in cooling capacity due to thermodynamic irreversibility and computing performance per unit energy consumption. Hence, we provide an approach that considers coefficient of performance COP_c, exergy efficiency η_{ex}, and a new metric, computing performance ratio CPR. In contrast to existing methods that consider one-dimensional workload distributions, the temperature predictions from a physics-based zonal model are used to optimize cooling for two-dimensional workload distributions in a multi-rack DC. The investigation reveals physics associated with two-dimensional workload management for multi-rack DCs, provides a framework for trade-offs between COP_c, η_{ex}, and CPR, explains the influence of IT load factor LF on different objectives, and describes how parameters obtained from single- and multi-objective problems can vary. Our findings show that COP_c, and η_{ex} can be improved by up to 20% and 8% by regulating the chilled water temperature and airflow setpoints while increasing the LF degrades the CPR by 7.5%. These results enable an extended approach for heterogeneous LF management in large-scale DCs.

Nomenclature

	Uppercase letters		*Lowercase letters*
A	Contact area between two fluids in the heat exchanger (m^2)	t	Time (s)
C_p	Specific heat capacity (J kg^{-1} K^{-1})	u	Utilization of a server zone
N_{cu}	Number of in-row cooling units		
N_p	Number of multi-rack DC pods		*Subscripts and superscripts*
N_r	Number of racks in the data center	a	Air
N_s	Number of servers in a zone	amb	Ambient
N_z	Number of zones in a rack	b	Back chamber
P	Pressure (Pa)	br	Brushes
$\dot{P}$	Power consumption (kW)	ch	Chiller
Q	Heat load (kW)	$cool$	Overall cooling system
$\dot{Q}$	Volume flowrate (m^3 s^{-1})	e	Server exhaust
R	Flow resistance (Pa m^{-3} s)	ex	Exergy
T	Absolute temperature	f	Front chamber
T_c	Cold-side temperature (K)	hx	Heat exchanger
T_g	ASHRAE guideline temperature (°C)	i	Horizontal index across racks
T_h	Hot-side temperature	j	Vertical index across zones
U	Overall heat transfer coefficient (W m^{-2} K^{-1})	r	Rack
V	Volume (m^3)	s	Server
X	Thermal mass (J K^{-1})	w	Water
		z	Zone
	Greek letters		*Abbreviations*
η	Efficiency	$ASTD$	Active server temperature distribution (°C)
ρ	Density (kg m^{-3})	COP_c	Co-efficient of performance of the cooling cycle
$\dot{\psi}$	Exergy destruction (kW)	CPR	Computing performance ratio
Δt	Time step (s)	CPR_m	Mean computing performance ratio
		LF	Load factor

1. Introduction

Data centers (DCs) and high-performance computing (HPC) clusters nowadays routinely process workloads associated with analytics and machine learning applications. For actionable use, high-performance computing infrastructure with low latencies is necessary. Since heat dissipation from DCs and HPC clusters has increased significantly with the use of multi-core processors and three-dimensional chip stacking, thermal and workload management requires adequate cooling at low cost. There are several thermal and workload management strategies to address operational expenditure [1, 2], chip thermal reliability [3], computing performance [4], latency [5], cooling architecture [6, 7], and waste heat harnessing [8-10].

Thermally-aware workload management and cooling is an integrated approach that considers interrelated issues, such as DC operational cost, chip thermal reliability, computing performance, and cooling architecture. The thermal reliability of computing chips is degraded because of (1) transient temperature fluctuations that diminish their lifetimes and (2) steady-state operating temperatures that rise above the critical allowable chip temperature and induce thermal shutdown. These thermal issues can be addressed by utilizing chip temperature-aware and cold aisle temperature-aware workload management approaches [11]. Other workload scheduling approaches address thermal guidelines and operational expenditure by minimizing heat recirculation across the cold and hot air streams in a DC [12], diminishing hot spots among neighboring servers [13], and lowering temperature nonuniformities in server exhausts [14, 15] (see Table 1).

Although it is possible to ensure thermal reliability while minimizing DC operational expenditure, existing temperature-based methodologies do not address the reduction in cooling capacity due to thermodynamic irreversibilities that result from uneven workload distributions and

cooling parameters. This deficiency can be addressed by approaches for exergy-based cooling management that minimize heat recirculation and bypass [16, 17], identify component level inefficiencies [6, 18], and optimize cooling parameters [19, 20]. However, there are few similar applications for workload management.

Recent investigations demonstrate the benefits of an exergy-based approach to select cooling architecture [6] and manage workload in air-cooled DCs [21]. The former advocates for the benefits of a modular DC cooling architecture over legacy raised-floor DCs, showing a 23% increase in the effective cooling capacity. The latter optimizes energy and exergy efficiency jointly for a single-rack modular air-cooled DC equipped with a rack-mountable cooling unit while simultaneously performing one-dimensional workload management and regulating cooling parameter setpoints. A comprehensive review of the state of the art in the thermal-aware workload management literature is presented in Table 1. Some important aspects highlighted in this table are number and type of objectives considered in the workload management framework, choice of the thermal model, type of the DC cooling architecture investigated, and whether the approach is multi-objective in nature to examine trade-offs between metrics.

Scaling up from a single-rack DC to a multi-rack system alters the airflow and thermal dynamics significantly. Because there are shared hot and cold airspaces in a multi-rack infrastructure, one-dimensional workload distributions obtained for a single-rack system cannot be scaled up for multi-rack DCs [21, 22]. Thus, workload distributions that vary in two dimensions must be obtained. Previous investigations have also not considered computing performance, i.e., Floating Point Operations Per Second (FLOPs) per Watt of power consumption [23, 24], simultaneously with energy and exergy efficiency. If an air-cooled DC is managed solely based on energy and exergy efficiencies, the computing performance is considerably degraded as

electronic chips become overheated. The actual FLOPs per Watt $\eta_{c,a}$ is determined by performing

LINPACK benchmark tests on a processor of interest [23]. Further, this quantity can be normalized

using the maximum achievable FLOPs per Watt $\eta_{c,i}$, which helps to define the dimensionless

metric computing performance ratio *CPR*. The value of $\eta_{c,a}$ is regulated by changing the (1) CPU

frequency through over- or under- clocking, (2) voltage, and (3) temperature [25, 26]. Although

simultaneous optimization of these parameters results in a global optimal value of *CPR*, we only

focus on thermal performance as per our objective.

We address the shortcomings of prior workload management approaches by proposing a

novel methodology to maximize (1) energy, (2) exergy, and (3) computing efficiencies for a five-

rack air-cooled DC equipped with two in-row cooling (IRC) units [22]. Energy and flow

interactions are considered across DC racks to obtain spatially two-dimensional temperature

distributions, which are used to solve a multi-objective genetic algorithm (MOGA)-based

optimization problem to optimize two-dimensional workload distributions and cooling parameters,

such as chilled water temperature and airflows of the IRC units.

As observed from Table 1, thermally-aware workload distribution algorithms require an

accurate dynamic thermal model for the DC. Several options are available, such as (a) data-driven

black-box models [27], (b) data-driven hybrid gray-box models [28, 29], (c) computational fluid

dynamics (CFD) simulation-based heat recirculation matrix (HRM) approaches [12], and (d)

physics-based zonal models [22, 30]. The first three require significant training data and

computational resources, and are the basis of prior workload scheduling algorithms. To circumvent

this problem, our framework utilizes an experimentally-validated, training-free, physics-based,

spatiotemporal zonal model to predict temperatures in a five-rack DC [22]. This physics-based

approach eliminates extrapolative temperature predictions, reduces computational time, and improves the accuracy of temperature predictions for new scenarios.

Table 1: Relevant state-of the art works in the area of thermal-aware workload and cooling management in DCs.

Ref.	Representation of an actual DC	Objectives or goals	Type of thermal model	Auxiliary sub-models	Optimization
[31]	No	• Maximizing utilization of solar energy	Heat recirculation matrix (HRM)	• Regression-based non-linear cooling energy model • Linear server energy model • Neural network based solar energy model	Single-objective optimization with linear constraints
[11]	Raised-floor DC	• Minimizing total energy consumption (including servers)	HRM	• Regression-based non-linear cooling energy model • Non-linear server energy model • Non-linear central processing unit (CPU) temperature model • Proper orthogonal decomposition (POD) based cold chamber temperature model	Single-objective optimization with non-linear constraints
[13]	Raised-floor DC	• Minimizing heat recirculation by assigning workloads according to cold chamber temperature and load of neighboring servers	Computational fluid dynamics (CFD) simulation	• Linear server energy model • Regression-based cold chamber temperature model	No
[32]	No	• Minimize hotspot temperature	HRM	• Linear server energy model • Regression-based cooling energy model • Job processing time models	Single-objective optimization with non-linear constraints
[33]	Raised-floor DC	• Minimizing peak temperature of servers • Minimizing job processing time of servers • Minimizing CO_2 emission	CFD simulation	• Thermal resistance capacitance based CPU temperature model • CFD data-driven cold aisle temperature predictor • Job processing time models	Single-objective optimization with non-linear constraints

		Objective	Thermal/airflow model	Other models	Optimization
[12]	Raised-floor DC	• Minimizing hot spot air temperature in cold chamber	HRM	• Linear server energy model • Non-linear regression based cooling energy model	Single-objective optimization with non-linear constraints
[34]	Raised-floor DC	• Minimizing total cooling energy • Minimize CPU temperature	CFD simulation	• Regression-based CRAC energy model • Thermal resistance capacitance based CPU temperature model • CFD data-driven cold aisle temperature predictor	Single-objective optimization with non-linear constraints
[15]	No	• Minimizing hotspot temperature in cold chamber	Regression-based	• Server thermal stress model	No
[35]	Raised-floor DC	• Minimizing total energy consumption (including servers)	Regression-based	• Non-linear regression based server energy model • Non-linear regression based cooling energy model	Single-objective optimization-based model predictive control
[36]	Raised-floor DC	• Maximizing utilization of solar photovoltaic energy • Maximizing utilization of free cooling	Regression-based	• Regression-based cooling energy model • Solar photovoltaic power forecasting model • Free cooling system model • Operational cost model	Single-objective optimization with linear and non-linear constraints
[14]	Raised-floor DC	• Maintain uniformity in the server exhaust temperatures • Reduce overcooling of the cold aisle	No	No	No
[20]	Raised-floor DC	• Minimizing energy consumption of cooling cycle • Minimizing exergy destruction in DC (including servers)	CFD simulation data-driven POD model	• Energy consumption and exergy destruction models of cooling cycle components (server, heat exchanger, fan, pump, chiller, and cooling tower)	Unconstrained single-objective optimization

[1]	single-rack DC with RMCU	• Minimizing cooling energy consumption	Flow network representation (FNR)-based zonal model	• Linear server energy model • Non-linear chiller power model • Non-linear fan power model	Single-objective optimization problem with both linear and non-linear constraints
[21]	single-rack DC with RMCU	• Minimizing cooling energy consumption • Maximizing exergy efficiency of cooling cycle	FNR-based zonal model	• Linear server energy model • Non-linear chiller power model • Linear fan model • Exergy destruction model of each component	Dual-objective optimization problem with both linear and non-linear constraints
Present work	Multi-rack DC with IRC units	• Minimize cooling energy consumption • Maximize exergy efficiency of cooling cycle • Maximize computing performance per unit energy consumption	FNR-based zonal model	• Linear server energy model • Non-linear CPU temperature model • Non-linear chiller power model • Non-linear fan power model • Exergy destruction model of each DC component • Non-linear computing performance per watt model	Tri-objective optimization problem with linear and non-linear constraints

To the best of our knowledge, this is the first work that develops a comprehensive workload and cooling management framework for multi-rack DCs cooled by IRC units. Considering the energy, exergy, and computing efficiency along with thermal reliability constraints allows for the exploration of insightful operational trade-offs. The proposed multi-objective optimization problem not only reveals the cooling and spatial workload dynamics, but also provides multi-objective trade-off diagrams applicable for real-world DC application.

With this background information, our sixfold contributions are:

- Proposing a new metric to describe computing performance degradation with rising CPU temperatures or thermal throttling. It has been observed in this work that with elevation of CPU temperatures the computing performance ratio can degrade by up to 7.5%.

- Explaining the trade-offs between energy and exergy-based cooling metrics and the computing performance metric. We solve three single- and one multi-objective optimization problems to better understand the nature of the objective function in decision making.

- Deriving a comprehensive formulation that couples our previous flow network-based temperature prediction model [22] for a five-rack air-cooled DC equipped with IRC units with energy, exergy, and computing efficiency models.

- Understanding of the relationship between workload distribution, cooling cycle operation, and thermal dynamics of a DC with shared hot and cold chambers.

- Explaining of the influence of the IT load factor for different optimization scenarios. We find that the load factor significantly alters the energy and computing efficiencies while the optimal value of exergy efficiency remains nearly unaltered by changing load factor.

- Utilizing the results for the five-rack case study to develop an extended scalable workload management approach for larger DCs.

11

The remaining sections are organized as follows. Section 2 develops a series of optimization problems with different objectives informed by the flow network-based temperature prediction model. Section 3 includes the results and physical insights obtained by solving the optimization problems. Finally, Section 4 provides concluding remarks and highlights salient findings.

2. Methodology

2.1. Physical layout and thermal model of the row-based cooling infrastructure

The multi-rack DC architectural layout with IRC units is described in Figure 1 [22]. The DC cooling infrastructure consists of five IT racks, each of them containing 15 2U servers (where 1U = 4.4 cm). The racks are stacked within an enclosure and share a common cold and hot chamber at the front and back of the IT racks, respectively. The cold chamber and hot chamber are separated by high-density air blocking brushes to prevent air from mixing. Two IRC units manufactured by RITTAL [37] supply the required cold air from two sides of the IT enclosure. Each IRC unit consists of an air-water fin-tube heat exchanger, three centrifugal fans, and a valve-based water flow control mechanism. A vapor compression refrigeration (VCR) chiller, equipped with an ambient air-cooled condenser [38], supplies the required chilled water to the IRC heat exchangers.

The thermal model adopts a zonal approach, which assumes that physical quantities inside each zone are spatially uniform [22]. This is a faster and reasonably accurate alternative to a full-field CFD simulation. A zone containing servers is modelled as a heat source whose magnitude depends on the IT stress level or utilization. Cooling unit fan zones supply predefined airflows at a specified temperature.
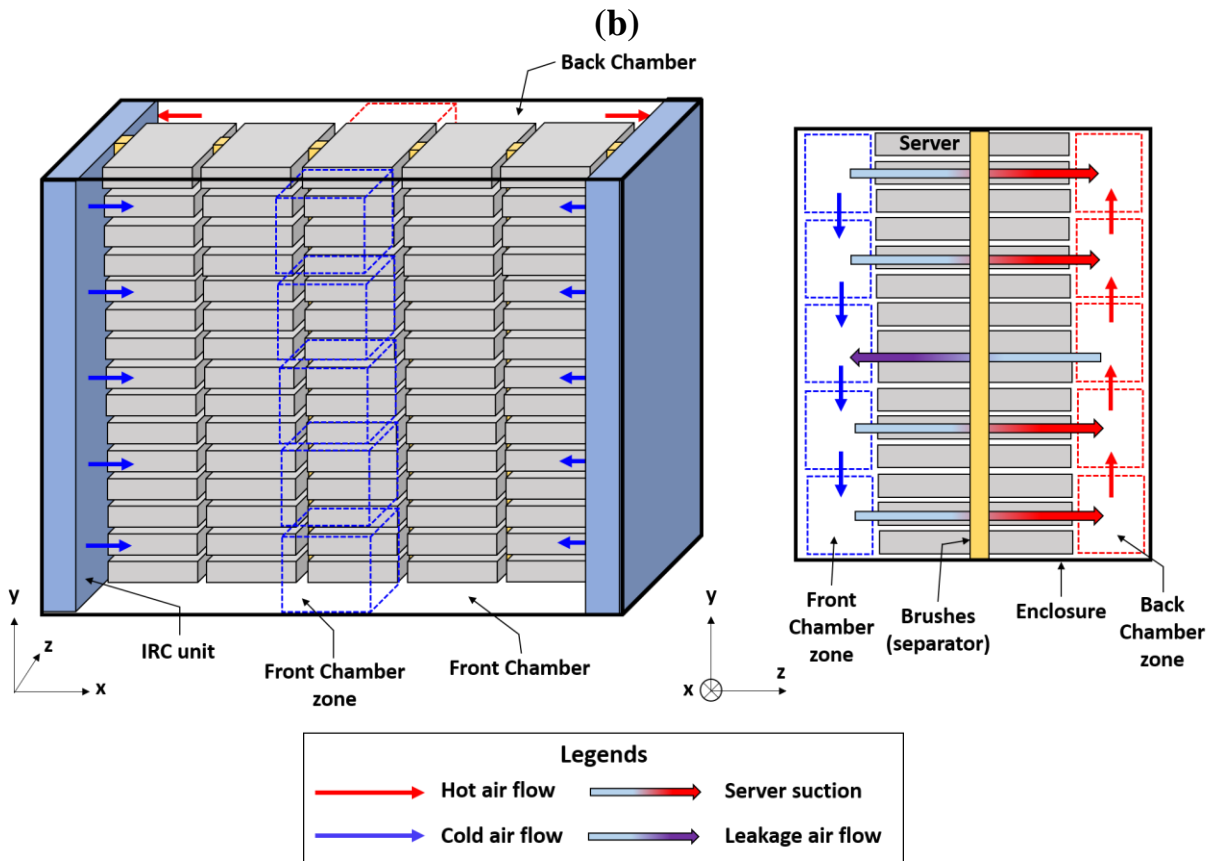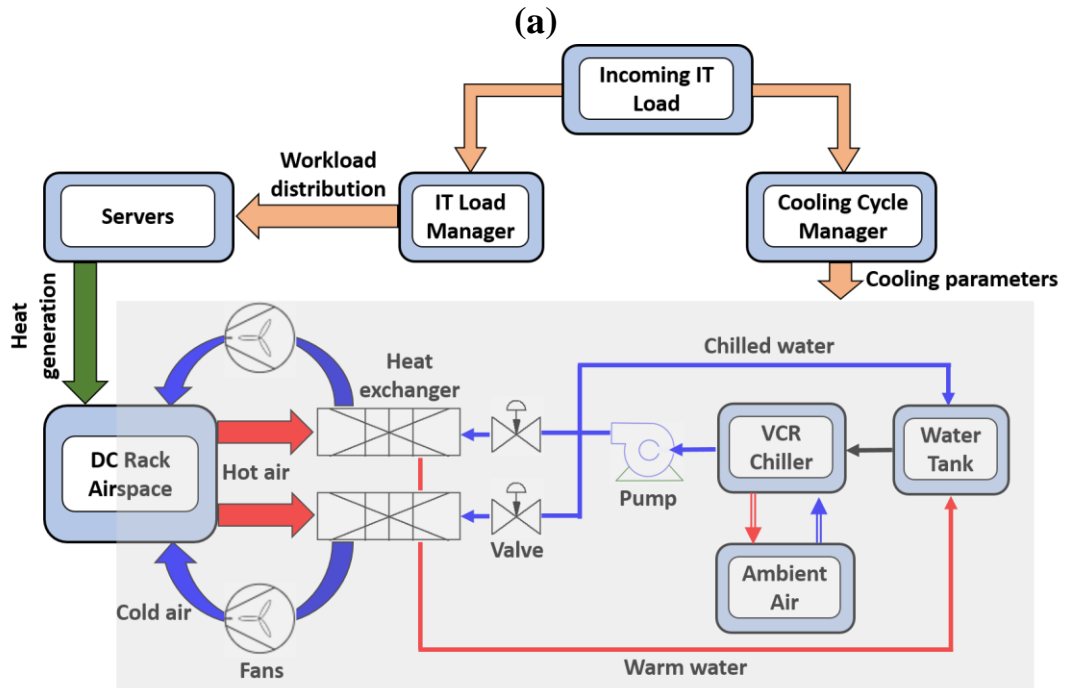
(a)

(b)

Legends

→ Hot air flow		⬛➡ Server suction	
→ Cold air flow		⬛➡ Leakage air flow	

Figure 1: (a) Process flow layout across different components for the DC case study, and (b) representative schematic of the DC infrastructure equipped with five server racks and two IRC units. The diagram on the left shows a three-dimensional representation of the DC, whereas the one on the right shows a sectional view representing salient airflows. A server rack is divided into five zones, where each zone consists of three 2U servers (1U = 4.4 cm). There are 35 zones (25 zones in front of servers and 5 zones in front of each IRC unit) in each of the front and back chambers.

There are several zones inside the DC enclosure, i.e., (1) in front of the IRC units or the cold air supply zone, (2) at the back of the IRC units or the warm air return zone, (3) cold air intake zones in front of the servers, (4) hot air exhaust zones at the back of servers, (5) each server itself, and (6) the IRC units. The cold chamber and hot chamber are partitioned into 25 zones of equal volume so that each consists of three 2U servers. The rationale for filling the IT racks in this manner is provided by the temperature prediction model, where each rack of 30U height must be filled (30U per rack = 5 zones per rack × 3 servers per zone × 2U server) [22, 30]. In addition, there are five cold air supply and return zones on each side of the enclosure, as shown in Figure 1b. Temperature prediction using the zonal framework is a two-step process, where a flow network representation (FNR) is used to calculate the pressures and airflows of all the zones. Thereafter, the pressure-flow data are used in energy balance equations to determine the zonal temperatures.

2.1.1. Airflow estimation of front (cold) and back (hot) chambers

The flow-field inside an enclosed DC is pressure-driven [22, 39], enabling an FNR to calculate the pressure-flow characteristics. The FNR is based on our previous work for a five-rack DC with two IRC units, as shown in Figure 2 [22]. IRC zones are represented as sources of airflow $\dot{Q}_a$, whereas the server airflows are denoted by $\dot{Q}_{i,j}^z$. The horizontal flow transport resistances in the front and back chambers are R_H^f and R_H^b, respectively, whereas the vertical flow transport resistances for the front and back chambers are R_V^f and R_V^b. The high-density air blocking brushes are porous

separation media enabling momentum and energy flux transport across the two chambers, which can be represented by a flow resistance R_{br}, values for which have been reported [22]. Since the enclosure is air tight, there are no flow interactions across the rack and the room (ambient).
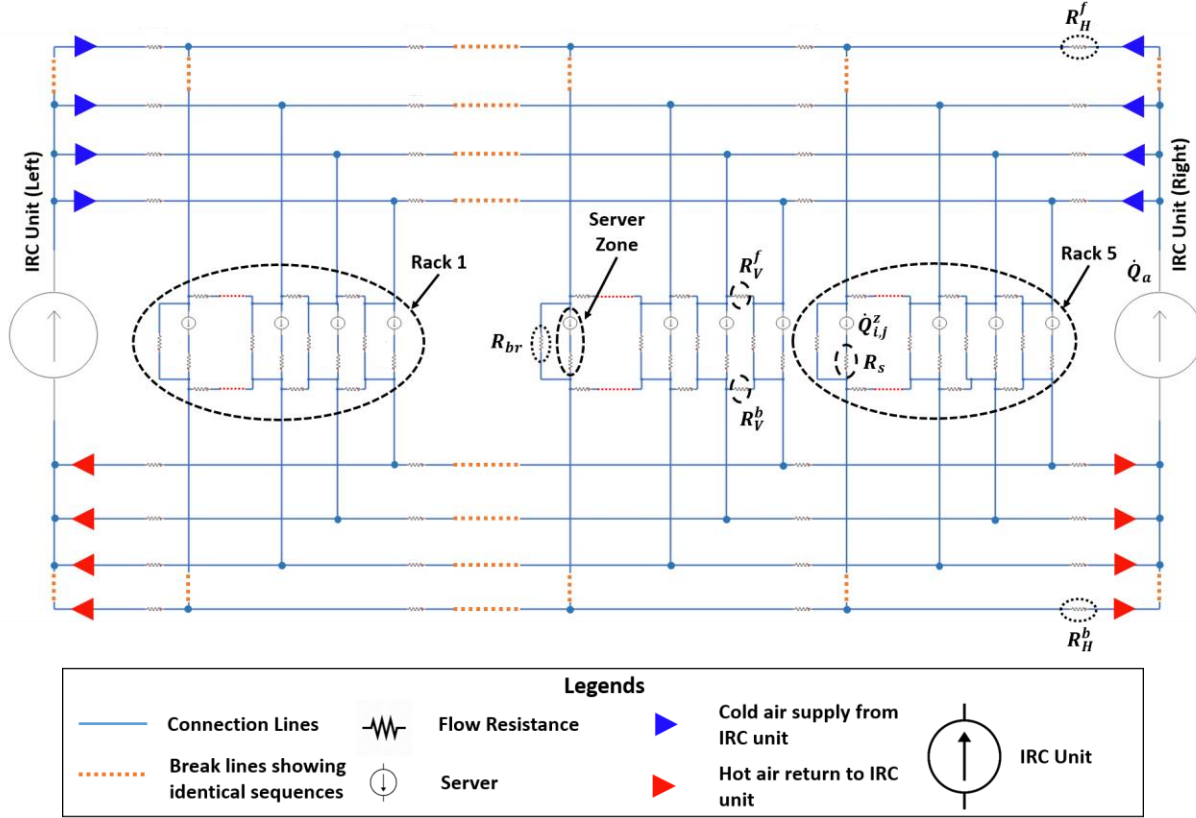
Figure 2: Generalized flow network representation (FNR) of the DC infrastructure for the case study with a total of 75 2U servers and 2 IRC units. The orange dotted lines represent identical sequences of flow resistances and servers in a simplified manner. Reproduced with permission from Ref. [22].

As a function of inlet air temperature, $T_{i,j}^{f}$, the airflow through a zone with N_s 2U servers is [30],

$$\dot{Q}_{i,j}^{z} = \begin{cases} N_s \times 0.01415 & \text{if} \quad T_{i,j}^{f} \le 25\,°\text{C} \\ N_s \times [0.01415 + (T_{i,j}^{f} - 25) \times 0.00142] & \text{if} \quad 25 < T_{i,j}^{f} < 35\,°\text{C} \end{cases} \tag{1}$$

For our system $N_s = 3$ as there are three 2U servers in each zone of an IT rack.

With flow resistances known, mass balance equations for the front chamber, back chamber, and heat-generating server zones can be formulated. The mass balances for zones in contact with active servers in the front and back chambers are expressed by Eqs. (2) and (3). The mass balances for the zones in an IRC cooling unit supply and return are calculated using Eqs. (4) and (5).

$$\alpha^f\left[P_{i+1,j}^f + P_{i-1,j}^f\right] + \beta^f\left[P_{i,j+1}^f + P_{i,j-1}^f\right] + \gamma P_{i,j}^b - (2\alpha^f + 2\beta^f + \gamma)P_{i,j}^f - \dot{Q}_{i,j}^z = 0, \tag{2}$$

$$\alpha^b\left[P_{i+1,j}^b + P_{i-1,j}^b\right] + \beta^b\left[P_{i,j+1}^b + P_{i,j-1}^b\right] + \gamma P_{i,j}^f - (2\alpha^b + 2\beta^b + \gamma)P_{i,j}^b + \dot{Q}_{i,j}^z = 0, \tag{3}$$

$$\alpha^f\left[P_{i+1,j}^f - P_{i,j}^f\right] - \frac{\dot{Q}_a}{N_z N_{cu}} = 0, \text{ and} \tag{4}$$

$$\alpha^b\left[P_{i+1,j}^b - P_{i,j}^b\right] + \frac{\dot{Q}_a}{N_z N_{cu}} = 0, \tag{5}$$

where $\alpha^f = 1/R_H^f$, $\alpha^b = 1/R_H^b$, $\beta^f = 1/R_V^f$, $\beta^b = 1/R_V^b$, $\gamma = 1/R_{br}$, $\dot{Q}_a$ the total airflow setpoint prescribed by the DC control system (split equally across two IRC units), $N_{cu} = 2$ is the number of IRC units, $N_z = 5$ the number of zones inside a rack, and P the pressure corresponding to the zone of interest. Equations (2)-(5) constitute a system of linear equations whose solution yields the spatial pressure distribution across different zones in the front and back chambers (see Appendix A1 for a detailed description).

2.1.2. Temperature estimation of front (cold) and back (hot) chambers

With the pressure distribution determined using FNR, the temperatures in the front and back chambers can be calculated. The transient energy balance for a server zone based on the forward time-marching method is,

$$\frac{X_s}{2}\left(\frac{T_{i,j}^e|_t - T_{i,j}^e|_{t-\Delta t}}{\Delta t} + \frac{T_{i,j}^f|_t - T_{i,j}^f|_{t-\Delta t}}{\Delta t}\right) = \rho_a C_{p,a} \dot{Q}_{i,j}^z \left(T_{i,j}^f|_{t-\Delta t} - T_{i,j}^e|_{t-\Delta t}\right) + \dot{P}_{i,j}^z, \tag{6}$$

where X_s is the thermal mass of a 2U server (available from the literature) [40], $T_{i,j}^e$ and $T_{i,j}^f$ are the server exhaust and inlet air temperatures, ρ_a the density of air, $C_{p,a}$ the specific heat capacity

of air, Δt the time step, and $\dot{P}_{i,j}^z$ the power consumption of the server zone with horizontal rack index i, and vertical zone index j. We note that a server's power consumption depends on its utilization, which is one of our decision variables for which the appropriate function is provided in Eq. (11).

The energy balance equations for the waterside and airside of the heat exchanger inside each IRC unit are expressed by Eqs. (7) and (8), respectively.

$$\frac{X_w}{2}\left(\frac{T_{h,w}^t - T_{h,w}^{t-\Delta t}}{\Delta t}\right) = \frac{UA}{2}\left(T_{h,a}^{t-\Delta t} + T_{c,a}^{t-\Delta t} - T_{c,w} - T_{h,w}^{t-\Delta t}\right) + \rho_w C_{p,w}\frac{\dot{Q}_w}{N_{cu}}\left(T_{c,w} - T_{h,w}^{t-\Delta t}\right), \text{ and} \tag{7}$$

$$\frac{X_a}{2}\left(\frac{T_{h,a}^t - T_{h,a}^{t-\Delta t}}{\Delta t} + \frac{T_{c,a}^t - T_{c,a}^{t-\Delta t}}{\Delta t}\right) = -\frac{UA}{2}\left(T_{h,a}^{t-\Delta t} + T_{c,a}^{t-\Delta t} - T_{c,w} - T_{h,w}^{t-\Delta t}\right) + \rho_a C_{p,a}\frac{\dot{Q}_a}{N_{cu}}\left(T_{h,a}^{t-\Delta t} - T_{c,a}^{t-\Delta t}\right). \tag{8}$$

Here $X_w = \rho_w C_{p,w} V_w$ and $X_a = \rho_a C_{p,a} V_a$ are the thermal masses of water and air inside the IRC unit, $\dot{Q}_w$ the total water flow prescribed by the DC control system (distributed equally across two IRC units), $T_{h,w}$ and $T_{c,w}$ the hot and chilled water temperatures, $T_{h,a}$ and $T_{c,a}$ the hot air return and cold air supply temperatures, UA the product of the universal heat transfer coefficient and the contact area between the two interacting fluid media, i.e., air and water. The value of UA as a function of $\dot{Q}_a$ and $\dot{Q}_w$ is obtained from our previous work [22].

For the zones considered within the front and back chambers, the energy balance equations are,

$$X_z\left(\frac{T_{i,j}^f\big|_t - T_{i,j}^f\big|_{t-\Delta t}}{\Delta t}\right) = \Omega_1^f + \Omega_2^f + \Omega_3^f + \Omega_4^f + \Omega_5^f + \Omega_6^f, \text{ and} \tag{9}$$

$$X_z\left(\frac{T_{i,j}^b\big|_t - T_{i,j}^b\big|_{t-\Delta t}}{\Delta t}\right) = \Omega_1^b + \Omega_2^b + \Omega_3^b + \Omega_4^b + \Omega_5^b + \Omega_6^b, \tag{10}$$

where $X_z = \rho_a C_{p,a} V_z$ denotes the thermal mass of zones in the front and back chambers and Ω_1 through Ω_6 are zonal flow interaction terms calculated using the pressure distribution. The expressions of these terms for different types of zones are provided in Table 2.

Table 2: Expressions for the zonal flow interaction terms $\Omega_{1\to6}^f$ and $\Omega_{1\to6}^b$ used in Eqs. (9) and (10), respectively.

$\Omega_{1\to6}^f$		$\Omega_{1\to6}^b$	
Ω_1^f (Horizontal flow transport in front chamber)		Ω_1^b (Horizontal flow transport in back chamber)	
$\left[P_{i+1,j}^f - P_{i,j}^f\right] \geq 0$	$\rho_a C_{p,a} \alpha^f \left(P_{i+1,j}^f - P_{i,j}^f\right) T_{i+1,j}^f$	$\left[P_{i+1,j}^b - P_{i,j}^b\right] \geq 0$	$\rho_a C_{p,a} \alpha^b \left(P_{i+1,j}^b - P_{i,j}^b\right) T_{i+1,j}^b$
$\left[P_{i+1,j}^f - P_{i,j}^f\right] < 0$	$\rho_a C_{p,a} \alpha^f \left(P_{i+1,j}^f - P_{i,j}^f\right) T_{i,j}^f$	$\left[P_{i+1,j}^b - P_{i,j}^b\right] < 0$	$\rho_a C_{p,a} \alpha^b \left(P_{i+1,j}^b - P_{i,j}^b\right) T_{i,j}^b$
Ω_2^f (Horizontal flow transport in front chamber)		Ω_2^b (Horizontal flow transport in back chamber)	
$\left[P_{i-1,j}^f - P_{i,j}^f\right] \geq 0$	$\rho_a C_{p,a} \alpha^f \left(P_{i-1,j}^f - P_{i,j}^f\right) T_{i-1,j}^f$	$\left[P_{i-1,j}^b - P_{i,j}^b\right] \geq 0$	$\rho_a C_{p,a} \alpha^b \left(P_{i-1,j}^b - P_{i,j}^b\right) T_{i-1,j}^b$
$\left[P_{i-1,j}^f - P_{i,j}^f\right] < 0$	$\rho_a C_{p,a} \alpha^f \left(P_{i-1,j}^f - P_{i,j}^f\right) T_{i,j}^f$	$\left[P_{i-1,j}^b - P_{i,j}^b\right] < 0$	$\rho_a C_{p,a} \alpha^b \left(P_{i-1,j}^b - P_{i,j}^b\right) T_{i,j}^b$
Ω_3^f (Vertical flow transport in front chamber)		Ω_3^b (Vertical flow transport in back chamber)	
$\left[P_{i,j+1}^f - P_{i,j}^f\right] \geq 0$	$\rho_a C_{p,a} \beta^f \left(P_{i,j+1}^f - P_{i,j}^f\right) T_{i,j+1}^f$	$\left[P_{i,j+1}^b - P_{i,j}^b\right] \geq 0$	$\rho_a C_{p,a} \beta^b \left(P_{i,j+1}^b - P_{i,j}^b\right) T_{i,j+1}^b$
$\left[P_{i,j+1}^f - P_{i,j}^f\right] < 0$	$\rho_a C_{p,a} \beta^f \left(P_{i,j+1}^f - P_{i,j}^f\right) T_{i,j}^f$	$\left[P_{i,j+1}^b - P_{i,j}^b\right] < 0$	$\rho_a C_{p,a} \beta^b \left(P_{i,j+1}^b - P_{i,j}^b\right) T_{i,j}^b$
Ω_4^f (Vertical flow transport in front chamber)		Ω_4^b (Vertical flow transport in back chamber)	
$\left[P_{i,j-1}^f - P_{i,j}^f\right] \geq 0$	$\rho_a C_{p,a} \beta^f \left(P_{i,j-1}^f - P_{i,j}^f\right) T_{i,j-1}^f$	$\left[P_{i,j-1}^b - P_{i,j}^b\right] \geq 0$	$\rho_a C_{p,a} \beta^b \left(P_{i,j-1}^b - P_{i,j}^b\right) T_{i,j-1}^b$
$\left[P_{i,j-1}^f - P_{i,j}^f\right] < 0$	$\rho_a C_{p,a} \beta^f \left(P_{i,j-1}^f - P_{i,j}^f\right) T_{i,j}^f$	$\left[P_{i,j-1}^b - P_{i,j}^b\right] < 0$	$\rho_a C_{p,a} \beta^b \left(P_{i,j-1}^b - P_{i,j}^b\right) T_{i,j}^b$
Ω_5^f (Flow transport through brushes in front chamber)		Ω_5^b (Flow transport through brushes in back chamber)	
$\left[P_{i,j}^b - P_{i,j}^f\right] \geq 0$	$\rho_a C_{p,a} \gamma \left(P_{i,j}^b - P_{i,j}^f\right) T_{i,j}^b$	$\left[P_{i,j}^f - P_{i,j}^b\right] \geq 0$	$\rho_a C_{pa} \gamma \left(P_{i,j}^f - P_{i,j}^b\right) T_{i,j}^f$
$\left[P_{i,j}^b - P_{i,j}^f\right] < 0$	$\rho_a C_{p,a} \gamma \left(P_{i,j}^b - P_{i,j}^f\right) T_{i,j}^f$	$\left[P_{i,j}^f - P_{i,j}^b\right] < 0$	$\rho_a C_{pa} \gamma \left(P_{i,j}^f - P_{i,j}^b\right) T_{i,j}^b$
Ω_6^f (Flow through active server)		Ω_6^b (Flow through active server)	
$-\rho_a C_{pa} \dot{Q}_{i,j}^s T_{i,j}^f$		$\rho_a C_{pa} \dot{Q}_{i,j}^s T_{i,j}^e$	

Equations (6)-(10) are solved by forward time marching to determine the temperature distributions for the zones in front and back chambers [22].

2.2. Objective 1: Energy consumption

The energy consumption in a DC consists of two components: (1) the servers and (2) the cooling cycle. Intuitively, the power consumption of a server is a composite function of its utilization and the inlet air temperature [41]. However, since changing the inlet air temperature by 40% alters the

server energy consumption by only 1% [42], we assume that the energy consumption attributed to a server is solely a function of its utilization. The total IT energy consumption inside the DC can therefore be expressed as,

$$\dot{P}_{IT} = \sum_{j=1}^{N_z} \sum_{i=1}^{N_r} \dot{P}_{i,j}^z = \sum_{j=1}^{N_z} \sum_{i=1}^{N_r} N_s [A_1 + A_2 u_{i,j}^z], \tag{11}$$

where the number of racks $N_r = 5$, number of servers per zone $N_s = 3$, and the number of zones in a rack $N_z = 5$. The server power model constants $A_1 = 223.4$ and $A_2 = 154.5$ are obtained from the datasheet of an HP ProLiant DL360 G5 server with two Intel Xeon E5-2697 v3 processors [43]. We assume this particular server to be employed solely throughout our DC.

The energy consumption of the cooling cycle has three components: (1) fans, (2) VCR chiller, and (3) pumps. The DC architecture under study is equipped with a fixed speed pump with valve-based flowrate control. Since the third component is invariant across different operational conditions and cannot be optimized, we only optimize the energy consumption of the fans inside the IRC units and the VCR chiller. The total energy consumption of the cooling cycle that can be optimized is,

$$\dot{P}_{cool} = \dot{P}_f + \dot{P}_{ch}. \tag{12}$$

The fan energy consumption for the RITTAL IRC units can be expressed as [22],

$$\dot{P}_f = N_{cu} \left[B_1 + B_2 \left(\frac{\dot{Q}_a}{N_{cu}} \right) + B_3 \left(\frac{\dot{Q}_a}{N_{cu}} \right)^2 \right], \tag{13}$$

where $B_1 = 480$, $B_2 = -3073$, and $B_3 = 6031$ are fan model constants [22]. We note that fan energy consumption models can be parabolic, cubic, or linear for different manufacturers and classes of fans.

While there are several options for calculating the energy consumption of the VCR chiller, we utilize the well-known Gordon-Ng universal chiller model [44] for its ease of use and low

computational requirement and high accuracy across a wide range of heat loads. The model has the form,

$$\dot{P}_{ch} = \frac{\dot{Q}_{ch} + C_1 T_{c,w} T_{amb} + C_2 (T_{amb} - T_{c,w})}{T_{c,w} - C_3 \dot{Q}_{ch}} - \dot{Q}_{ch}, \tag{14}$$

where $\dot{Q}_{ch}$ is the heat load on the chiller evaporator, i.e., the server heat load, $T_{c,w}$ the chilled water setpoint prescribed by the DC control system, T_{amb} the ambient air temperature entering the chiller condenser, and $\dot{P}_{ch}$ the power consumption of the chiller. All temperatures in Eq. (14) are expressed in units of K, whereas $\dot{P}_{ch}$ and $\dot{Q}_{ch}$ are in kW. To evaluate the model constants C_1 to C_3, performance data of the commercially available TRANE CGA120 10 Tons chiller is used [38]. The constants evaluated using multivariate linear regression are $C_1 = 0.0092$, $C_2 = 8.953$, and $C_3 = 0.649$. The value of T_{amb} is taken as 297.04 K from the chiller performance datasheet.

Finally, the performance of the DC cooling system from a 1st law of thermodynamics perspective can be represented by the coefficient of performance COP_c,

$$COP_c = \frac{\dot{P}_{IT}}{\dot{P}_{cool}}. \tag{15}$$

Investigators have previously considered the energy-based objective function during joint workload management and cooling control [1, 27]. Our first goal is to maximize COP_c by minimizing $\dot{P}_{cool}$ for a prescribed IT load $\dot{P}_{IT}$.

2.3. Objective 2: Exergy destruction

In an air-cooled DC equipped with IRC units, the overall exergy loss can be separated into (1) $\dot{\psi}_{ch}$ in the VCR chiller, (2) $\dot{\psi}_{hx}$ in the IRC air-water heat exchangers, (3) $\dot{\psi}_f$ in the fans, and (4) $\dot{\psi}_{serv}$ in the servers. Since the server exergy loss component due to heat generation is determined by the

total computing load, which we consider as input data, it cannot be optimized. Therefore, the controllable exergy loss $\dot{\psi}_{cool}$ consists of the three cooling cycle components,

$$\dot{\psi}_{cool} = \dot{\psi}_f + \dot{\psi}_{hx} + \dot{\psi}_{ch}. \tag{16}$$

The exergy loss in the chiller is [6, 20],

$$\dot{\psi}_{ch} = \rho_w C_{p,w} \dot{Q}_w T_{amb} \ln\left(\frac{T_{c,w}}{T_{h,w}}\right) + \rho_a C_{p,a} \dot{Q}_{cf} T_{amb} \ln\left(\frac{T_{h,amb}}{T_{amb}}\right). \tag{17}$$

Here $\dot{Q}_{cf}$ is the airflow through the condenser fans obtained from the chiller datasheet [38] and $T_{h,amb}$ is the hot air temperature exhausted to the environment through the chiller condenser.

The exergy loss in the IRC heat exchanger,

$$\dot{\psi}_{hx} = \rho_a C_{p,a} \dot{Q}_a \left[(T_{h,a} - T_{c,a}) - T_{amb}\ln\left(\frac{T_{h,a}}{T_{c,a}}\right)\right] + \rho_w C_{p,w} \dot{Q}_w \left[(T_{c,w} - T_{h,w}) - T_{amb}\ln\left(\frac{T_{c,w}}{T_{h,w}}\right)\right]. \tag{18}$$

That in the fans inside the IRC units is a function of airflow,

$$\dot{\psi}_f = (1 - \eta_f) N_{cu} \left[B_1 + B_2\left(\frac{\dot{Q}_a}{N_{cu}}\right) + B_3\left(\frac{\dot{Q}_a}{N_{cu}}\right)^2\right], \tag{19}$$

where the fan efficiency $\eta_f = 0.604$ is obtained from the datasheet of the IRC unit manufactured by RITTAL [37]. The exergy efficiency of the DC cooling system,

$$\eta_{ex} = \left(1 - \frac{\dot{\psi}_{cool}}{\dot{\psi}_{in}}\right) \times 100, \tag{20}$$

where the exergy input to the cooling cycle is further evaluated by,

$$\dot{\psi}_{in} = \dot{P}_f + \dot{P}_{ch} + \rho_a C_{p,a} \dot{Q}_a \left[(T_{h,a} - T_{amb}) - T_{amb}\ln\left(\frac{T_{h,a}}{T_{amb}}\right)\right]. \tag{21}$$

To reduce thermodynamic irreversibility during operation and maximize effective utilization of cooling capacity, η_{ex} should be maximized [20].

2.4. Objective 3: Computing efficiency

The computing efficiency of a server or a processor can be defined in various ways, where we choose the performance per Watt [23, 24], i.e., $\eta_{c,a}$ is calculated as GFLOPs (Giga Floating Point Operations per Second) per unit power consumption in Watts. Although there are several possible ways of maximizing $\eta_{c,a}$, we focus on the influence of CPU temperature $T_{i,j}^{CPU}$ on $\eta_{c,a}$. Experimental evidence shows that $\eta_{c,a}$ for Intel Xeon E5-2697 v3 processor is linearly dependent on $T_{i,j}^{CPU}$, i.e.,

$$\eta_{c,a} = D_1 + D_2 T_{i,j}^{CPU}, \tag{22}$$

where the constants $D_1 = 3.0$ and $D_2 = -6.9 \times 10^{-3}$ are obtained from a LINPACK benchmark case study performed by Druzhinin et al. [24] for Intel Xeon E5-2697 v3 processors.

The maximum achievable computing efficiency $\eta_{c,i}$ of a DC depends on computing cores per CPU, maximum frequency in GHz, FLOPs/cycle of operation, and thermal design power (TDP) of the computing processor,

$$\eta_{c,i} = \frac{racks \times \frac{servers}{rack} \times \frac{CPUs}{server} \times \frac{cores}{CPU} \times \frac{cycles}{second} \times \frac{FLOPs}{cycle}}{racks \times \frac{servers}{rack} \times \frac{CPUs}{server} \times TDP}. \tag{23}$$

A dimensionless metric, computing performance ratio CPR is defined as,

$$CPR = \frac{\eta_{c,a}}{\eta_{c,i}}. \tag{24}$$

An increase in $T_{i,j}^{CPU}$ causes $\eta_{c,a}$ to decrease which leads to a corresponding decrease in CPR (see Eqs. (22) and (24)). This reduction can be represented by linear, quadratic, or cubic polynomials that depend on the type and model of the CPU [25]. To deliver a fixed computing performance (in GFLOPs), a lower CPR corresponds to higher computing power (in Watts). Hence, CPR quantifies the loss in computing performance per unit power consumption due to CPU thermal

throttling. Other means to optimize CPR include changing the CPU clock speed (GHz) and supply voltage through dynamic voltage and frequency scaling (DVFS) [25, 26].

The metric CPR is meaningful when the DC has an imposed IT workload, i.e., $0 < LF \leq 1$, where $LF = \frac{\sum_{j=1}^{N_z} \sum_{i=1}^{N_r} u_{i,j}^z}{\sum_{j=1}^{N_z} \sum_{i=1}^{N_r} u_{i,j}^{max}}$. Although $LF = 0$, or zero IT load, provides the highest CPR, that condition is not realistic.

To determine CPR, it is essential to know the mean CPU temperature of each zone $T_{i,j}^{CPU}$ from the thermal model. We utilize a non-linear regression-based auxiliary equation for $T_{i,j}^{CPU}$ [45],

$$T_{i,j}^{CPU} = E_1 + E_2 u_{i,j}^z + E_3 T_{i,j}^f + E_4 \left(u_{i,j}^z\right)^2 + E_5 \left(u_{i,j}^z T_{i,j}^f\right), \tag{25}$$

where $u_{i,j}^z$ and $T_{i,j}^f$ are available from the zonal thermal model. The constants in Eq. (25) are determined by performing a non-linear regression using the data obtained from the datasheet [43] for an HP ProLiant DL360 G5 server with two Intel Xeon E5-2697 v3 processors. The resulting values are $E_1 = 20.2$, $E_2 = 59.1$, $E_3 = 0.76$, $E_4 = -8.1$, and $E_5 = -0.56$.

Finally, the mean computing performance ratio CPR_m of the five-rack DC is calculated by taking the average of the CPRs of all the zones,

$$CPR_m = F_1 + F_2 \frac{\sum_{j=1}^{N_z} \sum_{i=1}^{N_r} T_{i,j}^{CPU}}{N_z N_r}, \tag{26}$$

where the constants $F_1 = 0.75$, and $F_2 = -1.72 \times 10^{-3}$ are determined by performing a regression using the data obtained from [24]. Intuitively, higher CPU temperatures should increase the leakage current of a computing chip and decrease $\eta_{c,a}$ [23], resulting in lower CPR_m. Therefore, the aim is to maximize the value of CPR_m by jointly optimizing workload distribution and cooling system operating parameters.

2.5. Optimization problem formulation

Our objectives are to maximize (1) COP_c, (2) η_{ex}, and (3) CPR_m for the five-rack DC with two IRC units. To obtain the optimal cooling parameters and two-dimensional workload distributions, we solve four different optimization problems. The first three optimization problems employ three different objective functions, while in the fourth optimization problem all three objectives are optimized simultaneously. The structures of the optimization problems are presented in Table 3. The essential decision variables that regulate the objective functions are (1) distribution of zonal workload $u_{i,j}^z$, (2) chilled water temperature setpoint $T_{c,w}$, and (3) IRC unit airflow setpoint $\dot{Q}_a$. Two classes of servers are considered here, (1) active servers with $0 < u_{i,j}^z \leq 1$ and (2) idle servers with $u_{i,j}^z = 0$. Turning OFF an idle server, i.e., making it a passive server to save energy, changes the optimization framework significantly so that the continuous optimization problem becomes a combinatorial optimization problem [1]. Therefore, this consideration is beyond the scope of the present work. The total chilled water flow $\dot{Q}_w$ is fixed to a constant value of 15 GPM, since the optimal values are not sensitive to the water flow [21].

Table 3: The four different optimization problems considered.

Optimization 1	Optimization 2
$\underset{u_{i,j}^z, T_{c,w}, \dot{Q}_a}{\text{maximize}} \ [COP_c]$	$\underset{u_{i,j}^z, T_{c,w}, \dot{Q}_a}{\text{maximize}} \ [\eta_{ex}]$
s.t. $\frac{\sum_{j=1}^{N_z} \sum_{i=1}^{N_r} u_{i,j}^z}{\sum_{j=1}^{N_z} \sum_{i=1}^{N_r} u_{i,j}^{max}} = LF$	s.t. $\frac{\sum_{j=1}^{N_z} \sum_{i=1}^{N_r} u_{i,j}^z}{\sum_{j=1}^{N_z} \sum_{i=1}^{N_r} u_{i,j}^{max}} = LF$
$\max\left(T_{i,j}^f\right) \leq T_g$	$\max\left(T_{i,j}^f\right) \leq T_g$
$10 \leq T_{c,w}(\text{°C}) \leq 20$	$10 \leq T_{c,w}(\text{°C}) \leq 20$
$1300 \leq \dot{Q}_a(\text{CFM}) \leq 2300$	$1300 \leq \dot{Q}_a(\text{CFM}) \leq 2300$
$0 \leq u_{i,j}^z \leq u_{i,j}^{max}, \ i = 1, \dots, N_r, \text{and } j = 1, \dots, N_z$	$0 \leq u_{i,j}^z \leq u_{i,j}^{max}, \ i = 1, \dots, N_r, \text{and } j = 1, \dots, N_z$

Optimization 3	Optimization 4
$\underset{u_{i,j}^z, T_{c,w}, \dot{Q}_a}{\text{maximize}} \ [CPR_m]$	$\underset{u_{i,j}^z, T_{c,w}, \dot{Q}_a}{\text{maximize}} \ [COP_c, \eta_{ex}, CPR_m]$
s.t. $\frac{\sum_{j=1}^{N_z} \sum_{i=1}^{N_r} u_{i,j}^z}{\sum_{j=1}^{N_z} \sum_{i=1}^{N_r} u_{i,j}^{max}} = LF$	s.t. $\frac{\sum_{j=1}^{N_z} \sum_{i=1}^{N_r} u_{i,j}^z}{\sum_{j=1}^{N_z} \sum_{i=1}^{N_r} u_{i,j}^{max}} = LF$
$\max\left(T_{i,j}^f\right) \leq T_g$	$\max\left(T_{i,j}^f\right) \leq T_g$
$10 \leq T_{c,w}(\text{°C}) \leq 20$	$10 \leq T_{c,w}(\text{°C}) \leq 20$
$1300 \leq \dot{Q}_a(\text{CFM}) \leq 2300$	$1300 \leq \dot{Q}_a(\text{CFM}) \leq 2300$
$0 \leq u_{i,j}^z \leq u_{i,j}^{max}, \ i = 1, \dots, N_r, \text{and } j = 1, \dots, N_z$	$0 \leq u_{i,j}^z \leq u_{i,j}^{max}, \ i = 1, \dots, N_r, \text{and } j = 1, \dots, N_z$

The optimization problems are multi-dimensional with both linear and nonlinear constraints. The first three optimization problems have single objectives and are solved using the *fmincon* function of MATLAB with a *sequential quadratic programming* solver. The fourth optimization problem has three objective functions and is solved using the MOGA-based solver *gamultiobj* in MATLAB. The first constraint for all the optimization problems is linear, ensuring that the DC load factor (*LF*), i.e., the ratio of current IT load to maximum capacity $u_{i,j}^{max}$, is set to a particular preset value. The second constraint ensures that the maximum air temperature in the cold (front) chamber is capped below the American society of Heating, Refrigeration, and Air-Conditioning Engineers (ASHRAE) guideline temperature $T_g = 27$ °C [46], which prevents server overheating, ensuring thermally reliable operation. The working range of the decision variables is

obtained from the component datasheets of the IRC unit [37] and VCR chiller [38]. For all the optimization problems, the convergence criterion is set to 10^{-6}.

3. Results and discussion

3.1. Impact of workload distribution and cooling parameters on front (cold) chamber temperature distribution

The temperature distribution in the cold chamber of an air-cooled DC is an essential feature of the cooling infrastructure. The thermal reliability of a server depends on the cold air intake temperature, which is very sensitive to the zonal utilization levels of servers $u_{i,j}^z$ and cooling parameters $T_{c,w}$ and $\dot{Q}_a$ [21]. Instead of examining the entire cold chamber temperature to assess thermal characteristics, we consider the metric active server temperature distribution ($ASTD$) [39],

$$ASTD = \text{mean}\left(T_{i,j}^f\right) + \text{stdev}\left(T_{i,j}^f\right). \tag{27}$$

The cold air temperature $T_{i,j}^f$ supplied by the IRC units depends on both $T_{c,w}$ and $\dot{Q}_a$ for a fixed $\dot{Q}_w$, whereas the spatial variance of $T_{i,j}^f$ is regulated by $\dot{Q}_a$ only. Therefore, we note that $ASTD$ can be regulated by altering $T_{c,w}$, $\dot{Q}_a$, and the distribution of $u_{i,j}^z$.

Table 4 and Figure 3 show the influence of jointly varying $T_{c,w}$, $\dot{Q}_a$, and the distribution of $u_{i,j}^z$ on the $ASTD$ and rack-height averaged cold chamber temperature distributions. Comparing cases A, B, and C reveals that simultaneously increasing $T_{c,w}$ and $\dot{Q}_a$ raises $ASTD$, bringing it closer to the maximum allowable cold chamber temperature of 27 °C [46]. This, in turn, minimizes the overcooling of servers in the vicinity of IRC units, as shown in Figure 3 (Cases A and C). Comparing cases C, D, and E shows that workload distribution has an insignificant effect on the $ASTD$ and temperature distribution.

26

Table 4: Parametric details of the cases presented in Figure 3 with LF = 0.5 and $\max\left(T_{i,j}^{f}\right) \leq$ 27 °C. Red and dark green colors are mapped for two extreme values of $u_{i,j}^{z}$, 1 and 0, respectively.

Case	Distribution of $u_{i,j}^{z}$ across zones							$T_{c,w}$ (°C)	$\dot{Q}_a$ (CFM)	$ASTD$ (°C)
	Uniform workload assignment									
		R1	**R2**	**R3**	**R4**	**R5**				
		0.5	0.5	0.5	0.5	0.5				
A	**IRC unit (Left)**	0.5	0.5	0.5	0.5	0.5	**IRC unit (Right)**	20	2153	26.04
		0.5	0.5	0.5	0.5	0.5				
		0.5	0.5	0.5	0.5	0.5				
		0.5	0.5	0.5	0.5	0.5				
	Uniform workload assignment									
		R1	**R2**	**R3**	**R4**	**R5**				
		0.5	0.5	0.5	0.5	0.5				
B	**IRC unit (Left)**	0.5	0.5	0.5	0.5	0.5	**IRC unit (Right)**	10	1754	23.08
		0.5	0.5	0.5	0.5	0.5				
		0.5	0.5	0.5	0.5	0.5				
		0.5	0.5	0.5	0.5	0.5				
	Uniform workload assignment									
		R1	**R2**	**R3**	**R4**	**R5**				
		0.5	0.5	0.5	0.5	0.5				
C	**IRC unit (Left)**	0.5	0.5	0.5	0.5	0.5	**IRC unit (Right)**	15	1930	24.53
		0.5	0.5	0.5	0.5	0.5				
		0.5	0.5	0.5	0.5	0.5				
		0.5	0.5	0.5	0.5	0.5				
	Workload assigned away from IRC units									
		R1	**R2**	**R3**	**R4**	**R5**				
		0	0.75	1	0.75	0				
D	**IRC unit (Left)**	0	0.75	1	0.75	0	**IRC unit (Right)**	15	1978	24.36
		0	0.75	1	0.75	0				
		0	0.75	1	0.75	0				
		0	0.75	1	0.75	0				
	Workload assigned close to IRC units									
		R1	**R2**	**R3**	**R4**	**R5**				
		1	0.25	0	0.25	1				
E	**IRC unit (Left)**	1	0.25	0	0.25	1	**IRC unit (Right)**	15	1867	24.77
		1	0.25	0	0.25	1				
		1	0.25	0	0.25	1				
		1	0.25	0	0.25	1				

To identify local hotspots in the multi-rack DC, we provide rack-height averaged temperature distributions for the cases presented in Table 4. The red dotted line in Figure 3 corresponds to the maximum allowable temperatures in each rack [46]. Since the 3rd rack (R3) is located farthest from both the IRC units, it experiences the highest cold air temperature. Two physical phenomena are identified as primary causes for the hotspot in rack R3: (1) this hotspot has a higher airflow path resistance being farthest from the IRC units (see Figure 2), which increases the temperature, and (2) the lower air supply from the IRC units towards R3 increases the possibility of hot-air recirculation from the back (hot) chamber to the front (cold) chamber, thus increasing the local temperature. Overall, the cold chamber temperature is an essential feature of the DC optimization framework since the maximum cold chamber temperature influences thermal reliability.
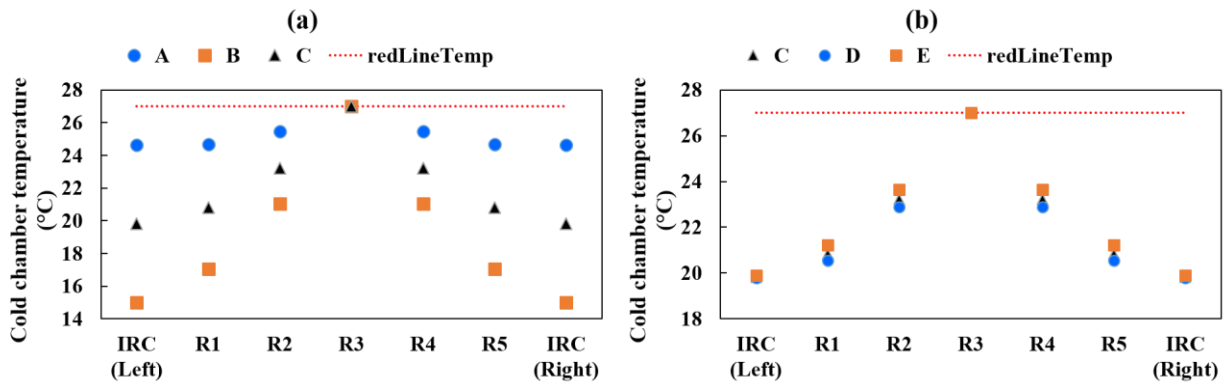

Figure 3: Influence of (a) cooling parameters $T_{c,w}$ and $\dot{Q}_a$ and (b) workload assignment on the rack height averaged cold chamber temperature distribution for the different cases listed in Table 4. The red dotted line in the figures denotes the maximum allowable temperature in the cold chamber.

3.2. Trade-offs in energy, exergy, and computing efficiency

To account for the interplay among different decision variables and objective functions, we first examine the parametric trade-offs across essential quantities such as (1) $u_{i,j}^z$, (2) $T_{c,w}$, (3) $\dot{Q}_a$, (4) LF, (5) COP_c, (6) η_{ex}, and (7) CPR_m, presented in Tables 5 and 6. For all cases, the maximum cold air temperature at the server inlets is maintained below 27 °C and $\dot{Q}_w = 15$ GPM. Table 5 shows the influence of coordinated regulation of $u_{i,j}^z$, $T_{c,w}$, and $\dot{Q}_a$ for $LF = 0.5$. For a constant LF, raising $T_{c,w}$ from 10 °C to 20 °C requires approximately 26% higher $\dot{Q}_a$ to maintain the maximum server inlet temperature below 27 °C. Doing so reduces the spatial air temperature variances in the cold chamber and improves η_{ex} by up to 3.5%. Although raising $T_{c,w}$ requires larger $\dot{Q}_a$, the overall COP_c of the DC improves by approximately 14% when $T_{c,w}$ is increased from 10 °C to 20 °C. This can be attributed to the fact that the energy savings obtained by operating the VCR chiller at a higher $T_{c,w}$ is significantly larger than what is required to drive the IRC fans [37, 38].

Assigning the server workloads closer to the IRC units (racks R1 and R5) requires up to 4.5% less $\dot{Q}_a$ due to the corresponding reduction in flow path resistance, which slightly improves COP_c (by approximately 1.5%), although η_{ex} is virtually unaltered when the distribution of $u_{i,j}^z$ changes. The mean computing performance ratio CPR_m is not significantly affected by jointly regulating the cooling parameters and workload distribution for a specific LF. Since the server inlet air temperature $T_{i,j}^f$ weakly influences $T_{i,j}^{CPU}$, CPR_m is unaltered [42]. Therefore, only two objectives, COP_c and η_{ex}, are controlled by altering the three decision variables $u_{i,j}^z$, $T_{c,w}$, and $\dot{Q}_a$.

Table 5: Influence of zonal workload assignments and cooling cycle decision variables on the three objectives for $LF = 0.5$ while satisfying the constraint $\max(T_{i,j}^f) \leq 27\,°C$. For all the cases $\dot{Q}_w = 15$ GPM. Red and dark green colors are mapped for the extreme values of $u_{i,j}^z$, 1 and 0, respectively.

Case	Distribution of $u_{i,j}^z$ across zones	$T_{c,w}$ (°C)	$\dot{Q}_a$ (CFM)	COP_c	η_{ex}(%)	CPR_m
	Uniformly distributed workload	10	1754	3.62	11.0	0.650
		12	1820	3.74	11.1	0.650
1	IRC unit (Left) — R1–R5 all 0.5 — IRC unit (Right)	14	1891	3.85	11.5	0.649
		16	1970	3.95	12.0	0.648
		18	2057	4.05	12.9	0.647
		20	2153	4.13	14.2	0.646
	Workload assigned close to IRC units	10	1674	3.66	10.1	0.651
		12	1745	3.78	10.3	0.651
2	IRC unit (Left) — R1=1, R2=0.25, R3=0, R4=0.25, R5=1 — IRC unit (Right)	14	1824	3.89	10.7	0.650
		16	1912	4.00	11.4	0.650
		18	2010	4.09	12.4	0.649
		20	2121	4.17	13.9	0.649
	Workload assigned away from IRC units	10	1816	3.59	11.7	0.655
		12	1877	3.70	11.8	0.654
3	IRC unit (Left) — R1=0, R2=0.75, R3=1, R4=0.75, R5=0 — IRC unit (Right)	14	1943	3.81	12.1	0.652
		16	2014	3.92	12.6	0.652
		18	2092	4.02	13.4	0.650
		20	2179	4.11	14.5	0.650

The influence of LF on the different objectives and decision variables is examined in Table 6. For all cases, the maximum temperature in the front chamber is maintained below 27 °C and $\dot{Q}_w$ is maintained at 15 GPM. Increasing LF from 0.2 to 0.8 shows that COP_c and η_{ex} improve by 23% and 6%, respectively, while the CPR_m degrades by approximately 6%. The degradation in the computing performance ratio CPR_m can be attributed to the elevated CPU temperature at higher LFs. As the VCR chiller operates efficiently from both energy and exergy perspectives at high LFs, both the 1st and 2nd law efficiencies improve, which improves overall COP_c and η_{ex}. Since LF is not under the control of the DC operator, CPR_m cannot be regulated by homogenous workload management across DC racks. Therefore, heterogeneous LF management across multi-rack DC systems should be adopted.

Tables 5 and 6 show that the three objectives are predominantly functions of $T_{c,w}$, $\dot{Q}_a$, and the distribution of $u_{i,j}^z$. Therefore, instead of adopting a brute force parametric variation approach, in subsequent sections we solve non-linear single- and multi-objective optimization problems to determine the optimum decision variables.

Table 6: Influence of *LF* on decision variables and objectives while satisfying the constraint $\max\left(T_{i,j}^{f}\right) \leq 27\,^{\circ}\mathrm{C}$. For all cases $\dot{Q}_w = 15$ GPM.

Distribution of $u_{i,j}^{z}$ across zones							$T_{c,w}$(°C)	$\dot{Q}_a$(CFM)	COP_c	η_{ex}(%)	CPR_m

Case 1: $LF = 0.2$

$T_{c,w}$(°C)	$\dot{Q}_a$(CFM)	COP_c	η_{ex}(%)	CPR_m
10	1661	3.42	10.2	0.673
12	1730	3.53	10.3	0.672
14	1807	3.63	10.7	0.671
16	1891	3.72	11.3	0.669
18	1985	3.80	12.3	0.668
20	2091	3.86	13.7	0.667

IRC unit (Left)	R1	R2	R3	R4	R5	IRC unit (Right)
	0.2	0.2	0.2	0.2	0.2	
	0.2	0.2	0.2	0.2	0.2	
	0.2	0.2	0.2	0.2	0.2	
	0.2	0.2	0.2	0.2	0.2	
	0.2	0.2	0.2	0.2	0.2	

Case 2: $LF = 0.5$

$T_{c,w}$(°C)	$\dot{Q}_a$(CFM)	COP_c	η_{ex}(%)	CPR_m
10	1754	3.62	11.0	0.651
12	1820	3.74	11.1	0.650
14	1891	3.85	11.5	0.649
16	1970	3.96	12.1	0.648
18	2057	4.05	12.9	0.647
20	2153	4.14	14.2	0.647

IRC unit (Left)	R1	R2	R3	R4	R5	IRC unit (Right)
	0.5	0.5	0.5	0.5	0.5	
	0.5	0.5	0.5	0.5	0.5	
	0.5	0.5	0.5	0.5	0.5	
	0.5	0.5	0.5	0.5	0.5	
	0.5	0.5	0.5	0.5	0.5	

Case 3: $LF = 0.8$

$T_{c,w}$(°C)	$\dot{Q}_a$(CFM)	COP_c	η_{ex}(%)	CPR_m
10	1829	3.75	11.5	0.632
12	1891	3.88	11.6	0.631
14	1959	4.00	12.0	0.631
16	2033	4.12	12.5	0.630
18	2113	4.23	13.4	0.629
20	2211	4.32	14.6	0.629

IRC unit (Left)	R1	R2	R3	R4	R5	IRC unit (Right)
	0.8	0.8	0.8	0.8	0.8	
	0.8	0.8	0.8	0.8	0.8	
	0.8	0.8	0.8	0.8	0.8	
	0.8	0.8	0.8	0.8	0.8	
	0.8	0.8	0.8	0.8	0.8	

3.3. Single-objective optimization results

3.3.1. Maximization of COP_c

The energy-based metric COP_c can be optimized by altering the cooling parameters, $T_{c,w}$ and $\dot{Q}_a$, and the zonal workload distribution $u_{i,j}^z$. The explicit optimization problem is shown in Table 3. The total chilled water flowrate $\dot{Q}_w$ is fixed at 15 GPM. The aim of the COP_c maximization problem is to find optimal values of $T_{c,w}$, $\dot{Q}_a$, and $u_{i,j}^z$ while maintaining the cold chamber temperature below 27 °C. Optimum values of decision variables and the objective are presented in Table 7 for five different *LF*s, 0.2, 0.35, 0.5, 0.65, and 0.8.

The COP_c maximization problem assigns the server workload closest to the IRC units for the entire range of *LF* values [1, 21]. As *LF* increases, the servers located near IRC units (in racks R1 and R5) are fully utilized, i.e., $u_{i,j}^z = 1$, which necessitates assigning additional incoming workloads to racks away from the IRC units (R2, R4, and R3). Even though *LF* is increased to 0.8, the farthest rack R3 remains unutilized since the workload capacities of racks R1, R2, R4, and R5 are sufficient to handle this *LF*. Increasing *LF* beyond 0.8 will utilize server zones in rack R3, which is placed farthest from both IRC units. This finding is in synergy with prior one-dimensional workload management algorithms that minimize the cooling energy consumption in air-cooled DCs [1]. However, we reveal the importance of the heterogeneity of $u_{i,j}^z$ inside a rack that creates a two-dimensional workload variation, which is essential for hotspot management. COP_c maximization results in a relatively high $T_{c,w} = 20\ °C$, which is invariant with changing *LF*. Raising $T_{c,w}$ reduces the energy consumption component of the chiller and maximizes COP_c. However, the total airflow $\dot{Q}_a$ of the fans inside IRC units varies non-linearly (see Eq. 13) with

changing *LF*. A higher *LF* results in higher heat generation from servers, when $\dot{Q}_a$ must be raised to bring the maximum cold chamber temperature below 27 °C.

Table 7: Optimal decision variables obtained from the COP_c maximization problem for different LF. Red and dark green colors are mapped for the extreme values of $u_{i,j}^z$, 1 and 0, respectively.

LF	Distribution of $u_{i,j}^z$ across zones							$T_{c,w}$ (°C)	$\dot{Q}_a$ (CFM)	COP_c

$LF = 0.2$ — IRC unit (Left) / IRC unit (Right)

	R1	R2	R3	R4	R5
	0.55	0.00	0.00	0.00	0.55
	0.41	0.00	0.00	0.00	0.34
	0.68	0.00	0.00	0.00	0.42
	0.55	0.00	0.00	0.00	0.48
	0.55	0.00	0.00	0.00	0.46

$T_{c,w} = 20$, $\dot{Q}_a = 2034$, $COP_c = 3.92$

$LF = 0.35$ — IRC unit (Left) / IRC unit (Right)

	R1	R2	R3	R4	R5
	0.97	0.00	0.00	0.00	0.77
	1.00	0.00	0.00	0.00	0.00
	0.76	0.00	0.00	0.00	1.00
	0.88	0.00	0.00	0.00	0.88
	0.88	0.00	0.00	0.00	0.86

$T_{c,w} = 20$, $\dot{Q}_a = 2054$, $COP_c = 4.08$

$LF = 0.5$ — IRC unit (Left) / IRC unit (Right)

	R1	R2	R3	R4	R5
	1.00	0.24	0.00	0.21	1.00
	1.00	0.29	0.00	0.30	1.00
	1.00	0.30	0.00	0.30	1.00
	1.00	0.13	0.00	0.14	1.00
	1.00	0.29	0.00	0.30	1.00

$T_{c,w} = 20$, $\dot{Q}_a = 2081$, $COP_c = 4.21$

$LF = 0.65$ — IRC unit (Left) / IRC unit (Right)

	R1	R2	R3	R4	R5
	1.00	0.58	0.00	0.77	1.00
	1.00	0.68	0.00	0.66	1.00
	1.00	0.34	0.00	1.00	1.00
	1.00	0.66	0.00	0.69	1.00
	1.00	0.38	0.00	0.50	1.00

$T_{c,w} = 20$, $\dot{Q}_a = 2107$, $COP_c = 4.32$

$LF = 0.8$ — IRC unit (Left) / IRC unit (Right)

	R1	R2	R3	R4	R5
	1.00	1.00	0.00	1.00	1.00
	1.00	1.00	0.00	1.00	1.00
	1.00	1.00	0.00	1.00	1.00
	1.00	1.00	0.00	1.00	1.00
	1.00	1.00	0.00	1.00	1.00

$T_{c,w} = 20$, $\dot{Q}_a = 2130$, $COP_c = 4.41$

A higher LF significantly improves COP_c (by up to 12.5%), since the VCR chiller operates more effectively at higher LFs [38]. Although COP_c maximization reduces cooling energy consumption, it does not necessarily diminish thermodynamic irreversibility in the DC cooling system during operation. This often leads to loss of available cooling capacity and further reduces η_{ex} [6, 20, 21].

3.3.2. Maximization of η_{ex}

To address the drawback of COP_c maximization from a 2nd law of thermodynamics perspective, the second optimization problem (see Table 3) maximizes η_{ex}. The nonlinear constrained optimization is solved using the methodology in Section 2.5. The resulting values of decision variables and optimized objective function values are presented in Table 8 for a wide range of LFs. In contrast to the conventional approach of assigning workloads to racks closest to the IRC units, the η_{ex} maximization problem partially distributes the server workload across the racks (see workload color maps in Table 8). A high value of $\dot{Q}_a$ is preferred since raising the airflow diminishes $\dot{\psi}_{cool}$ due to spatial air temperature gradients. Increasing $\dot{Q}_a$ also reduces the probability of hot air recirculation and hotspot formation in the cold chamber [21]. A low value of $T_{c,w}$ is preferred since, at lower chilled water temperatures, the 2nd law efficiency of the VCR chiller improves, and the heat transfer efficiency (or effectiveness) of the IRC heat exchanger is enhanced. As the LF changes, the cooling cycle variables $\dot{Q}_a$ and $T_{c,w}$ remain invariant while the workload distribution changes, resulting in η_{ex} maximization. The LF does not significantly affect (less than 2% difference) η_{ex} and the highest value of $\eta_{ex} = 18.6\%$ is observed for an $LF = 0.2$.

Table 8: Optimal decision variables obtained from the η_{ex} maximization problem for different *LF*. Red and dark green colors are mapped for the extreme values of $u_{i,j}^z$, 1 and 0, respectively.

LF	Distribution of $u_{i,j}^z$ across zones	$T_{c,w}$ (°C)	$\dot{Q}_a$ (CFM)	η_{ex} (%)

LF = 0.2, IRC unit (Left) ... IRC unit (Right), $T_{c,w}=10$, $\dot{Q}_a=2300$, $\eta_{ex}=18.6$

	R1	R2	R3	R4	R5
	0.00	0.15	0.03	0.15	0.11
	0.86	0.15	0.03	0.15	1.00
	0.01	0.27	0.02	0.27	0.28
	0.27	0.27	0.02	0.27	0.01
	0.05	0.27	0.02	0.27	0.05

LF = 0.35, IRC unit (Left) ... IRC unit (Right), $T_{c,w}=10$, $\dot{Q}_a=2300$, $\eta_{ex}=18.1$

	R1	R2	R3	R4	R5
	0.15	0.51	0.06	0.55	0.96
	0.19	0.59	0.00	0.56	0.17
	0.19	0.25	0.00	0.42	0.97
	0.21	0.41	0.03	0.21	0.99
	0.22	0.43	0.05	0.41	0.22

LF = 0.5, IRC unit (Left) ... IRC unit (Right), $T_{c,w}=10$, $\dot{Q}_a=2300$, $\eta_{ex}=17.6$

	R1	R2	R3	R4	R5
	0.66	0.25	0.00	0.55	0.73
	0.70	0.83	0.00	0.49	0.64
	0.60	1.00	0.00	1.00	0.68
	0.46	0.11	0.00	0.12	0.60
	0.64	0.92	0.00	0.92	0.61

LF = 0.65, IRC unit (Left) ... IRC unit (Right), $T_{c,w}=10$, $\dot{Q}_a=2300$, $\eta_{ex}=17.1$

	R1	R2	R3	R4	R5
	0.89	0.41	0.08	0.00	0.70
	0.69	0.71	0.03	0.01	0.75
	1.00	1.00	0.98	1.00	1.00
	1.00	1.00	0.69	1.00	1.00
	0.26	0.91	0.00	0.93	0.21

LF = 0.8, IRC unit (Left) ... IRC unit (Right), $T_{c,w}=10$, $\dot{Q}_a=2300$, $\eta_{ex}=16.7$

	R1	R2	R3	R4	R5
	1.00	1.00	0.38	1.00	1.00
	1.00	1.00	0.07	1.00	1.00
	1.00	1.00	0.00	0.98	1.00
	1.00	0.00	0.48	0.15	1.00
	1.00	1.00	0.94	1.00	1.00

The first two optimization problems maximize COP_c and η_{ex} of the cooling cycle from the perspective of the 1st and 2nd laws of thermodynamics, respectively. These two approaches reduce the cooling cycle operational expenditure and the loss of effective cooling capacity. However, they do not necessarily reduce overheating of the CPU, which degrades the value of the computing performance ratio CPR_m (see Eqs. (22)-(26)).

3.3.3. Maximization of CPR_m

The third optimization problem maximizes the computing performance per unit energy consumption by maximizing CPR_m (see Table 3). It is worth noting that CPR_m only captures the effects of computing performance degradation at elevated chip temperature (see Section 2.4). This approach is somewhat similar to CPU temperature-aware workload scheduling and cooling control, where the idea is to keep the CPU die temperature below a certain value [11]. The objective function CPR_m is represented as a function of the mean CPU temperatures of each zone $T_{i,j}^{CPU}$ (see Eqs. (22)-(26)). From Tables 5 and 6, we note that CPR_m is altered by changing $T_{c,w}$, $\dot{Q}_a$, the distribution of $u_{i,j}^z$, and LF. Therefore, the aim is to find $T_{c,w}$, $\dot{Q}_a$, and $u_{i,j}^z$ for a wide range of LF while keeping the cold chamber air temperature below 27 °C. Table 9 shows the optimal values of the decision variables and the objective function for various LF scenarios.

Table 9: Optimal decision variables obtained from the CPR_m maximization problem for different LF. Red and dark green colors are mapped for the extreme values of $u_{i,j}^z$, 1 and 0, respectively.

LF	Distribution of $u_{i,j}^z$ across zones							$T_{c,w}$ (°C)	$\dot{Q}_a$ (CFM)	CPR_m

LF = 0.2

		R1	R2	R3	R4	R5	
	IRC unit (Left)	1.00	0.00	1.00	0.00	0.00	IRC unit (Right)
		1.00	0.00	1.00	0.00	0.00	
		0.00	0.00	1.00	0.00	0.00	
		0.00	0.00	0.00	0.00	0.00	
		0.00	0.00	0.00	0.00	0.00	

$T_{c,w} = 10$, $\dot{Q}_a = 2300$, $CPR_m = 0.682$

LF = 0.35

		R1	R2	R3	R4	R5	
	IRC unit (Left)	1.00	0.00	0.00	0.00	0.00	IRC unit (Right)
		1.00	0.00	0.00	0.00	0.75	
		1.00	1.00	0.00	1.00	1.00	
		1.00	0.00	0.00	0.00	1.00	
		0.00	0.00	0.00	0.00	0.00	

$T_{c,w} = 10$, $\dot{Q}_a = 2300$, $CPR_m = 0.671$

LF = 0.5

		R1	R2	R3	R4	R5	
	IRC unit (Left)	1.00	0.00	0.00	1.00	1.00	IRC unit (Right)
		1.00	1.00	0.00	1.00	1.00	
		0.50	0.00	0.00	0.00	1.00	
		1.00	1.00	0.00	1.00	1.00	
		0.00	0.00	0.00	0.00	0.00	

$T_{c,w} = 10$, $\dot{Q}_a = 2300$, $CPR_m = 0.659$

LF = 0.65

		R1	R2	R3	R4	R5	
	IRC unit (Left)	1.00	1.00	0.00	1.00	1.00	IRC unit (Right)
		1.00	1.00	0.00	1.00	1.00	
		0.00	0.00	0.25	0.00	0.00	
		1.00	1.00	0.00	1.00	1.00	
		1.00	1.00	0.00	1.00	1.00	

$T_{c,w} = 10$, $\dot{Q}_a = 2300$, $CPR_m = 0.648$

LF = 0.8

		R1	R2	R3	R4	R5	
	IRC unit (Left)	1.00	0.00	1.00	0.00	1.00	IRC unit (Right)
		1.00	1.00	1.00	0.00	1.00	
		1.00	1.00	0.00	1.00	1.00	
		1.00	1.00	1.00	1.00	1.00	
		1.00	1.00	0.00	1.00	1.00	

$T_{c,w} = 10$, $\dot{Q}_a = 2300$, $CPR_m = 0.637$

A low $T_{c,w}$ and high $\dot{Q}_a$ are preferred since regulating these two variables reduces the cold air supply temperature to the servers $T_{i,j}^f$. As a result of lower cold air temperature at the server inlet, the CPU temperature decreases and improves CPR_m by less than 1%. The approach also distributes workload partially across the racks rather than assigning them closest to the IRC units for a wide range of LFs, as evident from the two-dimensional heatmaps of zonal utilization distribution (see Table 9). For the majority of zones, either $u_{i,j}^z = 0$ or $u_{i,j}^z = 1$ is preferred. Raising LF degrades the maximum achievable CPR_m since a larger LF is associated with elevated CPU temperatures ($> 65\ ^\circ\text{C}$). For example, increasing LF from 0.2 to 0.8 diminishes the CPR_m by approximately 6.6% as CPU temperatures increase with higher LFs. Thus, CPR_m is a weak function of $T_{c,w}$ and $\dot{Q}_a$, while it is strongly influenced by LF and the distribution of $u_{i,j}^z$ [42].

3.3.4. Summary of single-objective optimizations

The results obtained by solving the COP_c, η_{ex}, and CPR_m single-objective maximization problems for different values of LF are presented in Figure 4. As the LF for the DC increases, COP_c improvement is possible due to the higher energy efficiency of the VCR chiller [38]. An elevated LF raises the cooling load on the VCR chiller, moving it towards the designed cooling capacity of the chiller. On the other hand, changing LF has an insignificant effect (less than a 2% difference) on the maximum achievable η_{ex}, i.e., the exergy efficiency from the single-objective optimization problem is essentially independent of LF. The third optimization problem, CPR_m maximization, shows the influence of LF on the mean computing performance ratio (see Figure 4a). Increasing LF from 0.2 to 0.8 degrades the maximum achievable CPR_m by approximately 7.5% as $T_{i,j}^{CPU}$ is elevated. The lower values of CPR_m correspond to poor computing performance, i.e., lower GFLOPs per unit power consumption, resulting in higher latencies and increased energy

40

expenditure. The result is that the three different objectives cannot be achieved with similar combinations of decision variables and *LF*s. To address this problem, we solve a non-linear tri-objective optimization problem to address the trade-offs across objective functions and decision variables using a MOGA-based Pareto front approach.
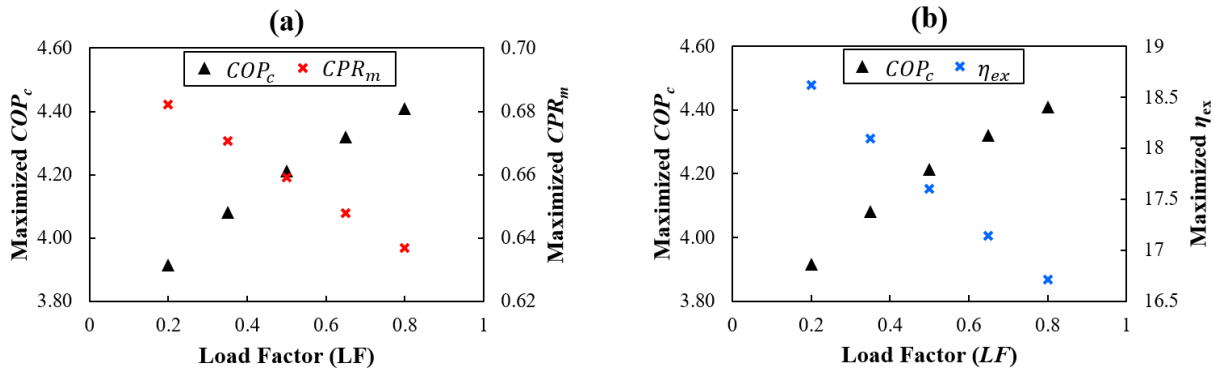

Figure 4: Effect of load factor (*LF*) on optimum values of three objective functions: (a) Variation of COP_c and CPR_m as a function of *LF*, (b) Variation of COP_c and η_{ex} as a function of *LF*.

3.4. Multi-objective optimization

To address the trade-offs between the three different single-objective optimization problems, the fourth optimization problem is MOGA-based, incorporating knowledge of all the three objective functions simultaneously (see Table 3). The tri-objective optimization problem is solved for five different *LF*s, 0.2, 0.35, 0.5, 0.65, and 0.8 leading to a three-dimensional Pareto front (or trade-off diagram). To better represent the relation between different objectives, we separate the three-dimensional Pareto front in Figure 5 into three different two-dimensional projections showing trends of (1) η_{ex} *vs.* COP_c, (2) CPR_m *vs.* COP_c, and (3) CPR_m *vs.* η_{ex}. In all trade-off diagrams, the "desired region" and the "undesired region" correspond to the regimes where both the objectives are simultaneously maximized and minimized, respectively. For each *LF*, a separate Pareto front is obtained, as shown in Figures 5a, b and c. Figure 5a reveals a trade-off between the energy-based metric COP_c and exergy-based metric η_{ex}. High values for both COP_c and η_{ex} can

only be achieved with higher LF when the VCR chiller operates close to its designed cooling capacity. As LF is increased from 0.2 to 0.8, the Pareto front shifts towards the desired region. Figure 5b suggests that when the LF is increased from 0.2 to 0.8, even though the COP_c improves by 20%, the CPR_m lowers by approximately 7.5%. Operation at a lower LF (for example, $LF =$ 0.2) stretches the Pareto optimal front of COP_c so that the DC operator can make a desired choice across a wider range than for a higher LF. Figure 5c shows the proportionality trade-off between CPR_m and. η_{ex}. At a certain LF, a high value of η_{ex} (approximately 18%) is achievable by regulating the cooling cycle parameters $T_{c,w}$ and $\dot{Q}_a$, which slightly enhances the CPR_m (up to 1%).
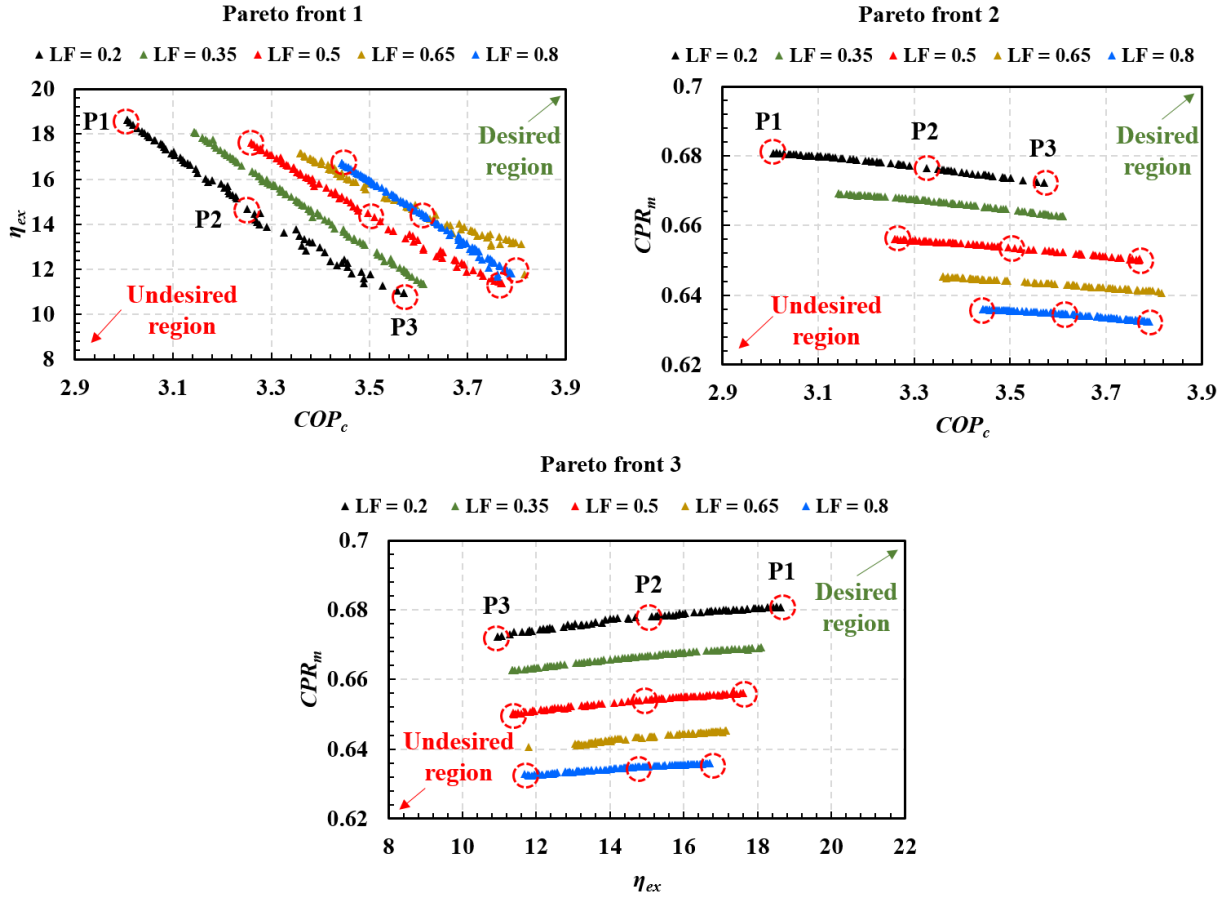
Figure 5: Pareto optimal fronts obtained by solving the multi-objective optimization problem while satisfying $T_g = 27\ ^\circ\text{C}$ for different *LF*s. The tri-axis Pareto front is separated into three different two-dimensional Pareto fronts: (1) η_{ex} *vs.* COP_c, (2) CPR_m *vs.* COP_c, and (3) CPR_m *vs.* η_{ex} for better representing the trade-offs across different objectives. The "desired region" and the "undesired region" are the regimes where both the objectives are simultaneously maximized and minimized, respectively.

To gain better insight into the interplay across decision variables and thermal behavior, we present the values of $T_{c,w}$, $\dot{Q}_a$, CPR_m, COP_c, η_{ex}, distributions of $u_{i,j}^z$, $ASTD$ and rack-height averaged temperature distribution for salient points across the Pareto fronts in Table 10, and Figures 6 and 7.

Table 10: Decision variables and objective function values for nine salient points marked on the Pareto optimal fronts presented in Figure 5.

LF	Point	$T_{c,w}$ (°C)	$\dot{Q}_a$ (CFM)	COP_c	η_{ex} (%)	CPR_m	$ASTD$ (°C)
	P1	10.0	2300	3.0	18.6	0.680	13.9
0.2	P2	10.7	2056	3.2	15.1	0.678	16.9
	P3	13.2	1804	3.6	10.9	0.672	23.2
	P1	10.0	2300	3.2	17.6	0.656	14.7
0.5	P2	11.0	2074	3.5	14.5	0.653	18.2
	P3	12.7	1855	3.8	11.4	0.650	23.6
	P1	10.0	2300	3.4	16.7	0.635	15.4
0.8	P2	10.4	2092	3.6	14.3	0.634	18.3
	P3	10.8	1877	3.8	11.8	0.632	22.8

Moving from P1 towards P3 on a particular Pareto front slightly affects the distribution of $u_{i,j}^z$, where P3 is associated with more server zones at $u_{i,j}^z = 1$. However, changing LF entirely alters the workload distribution to support a higher IT load (see Figure 6). Nevertheless, Table 10 shows that the cooling parameters $T_{c,w}$ and $\dot{Q}_a$ regulate the desired values of COP_c and η_{ex} for a specified LF. Moving from P1 towards P3 for a specific LF results in an increase in $T_{c,w}$ while simultaneously decreasing $\dot{Q}_a$. This raises the mean and variance of the cold chamber air temperature, as evident from the $ASTD$ and the rack height average temperature distribution presented in Table 10 and Figure 7, respectively. Although raising the mean cold air temperature is beneficial from the perspective of maximizing COP_c, increasing the spatial variance in the air temperature causes local hotspots, leading to a higher system irreversibility and reduced η_{ex}. Therefore, an intermediate point on the Pareto front can yield a desirable trade-off across COP_c and η_{ex}. As the LF increases, the extent of variation for $T_{c,w}$ and $\dot{Q}_a$ decreases, consequently yielding higher values of COP_c and η_{ex}. Although $ASTD$ is altered upon moving from P1 to P3 on a Pareto front, it is nearly unaffected by changing LF. Therefore, we conclude that LF has an insignificant effect on the cold chamber temperature distribution (see Figure 7). The third

objective, CPR_m, changes only by 1% on a Pareto front for a given LF. However, increasing the LF degrades the value of CPR_m by as much as 7%.
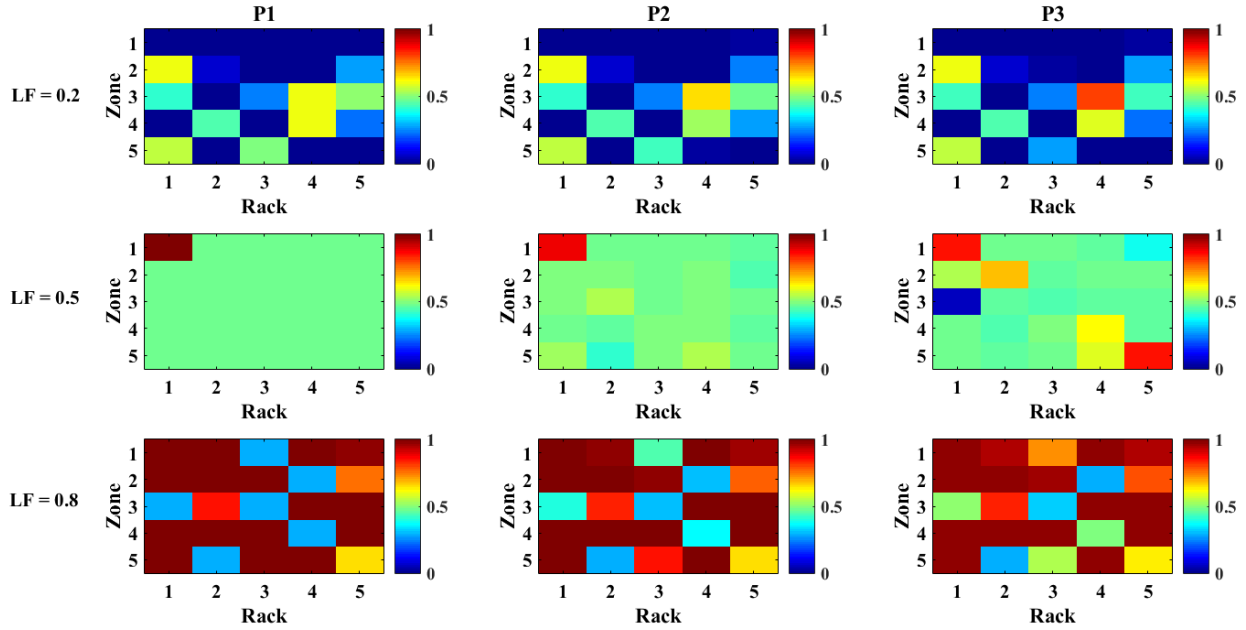

Figure 6: Two-dimensional distributions of zonal utilizations $u_{i,j}^z$ for nine different points marked on the Pareto fronts shown in Figure 5. The color bars are scaled for the extreme values of $u_{i,j}^z$, 0 and 1, respectively. This figure is to be interpreted in accordance with Table 10.

Examining the rack-height averaged temperature distribution (see Figure 7) for salient points on the Pareto fronts shows that for all LFs considered, the regime where P1 lies is associated with low cold chamber air temperature and lower variance of temperature across the racks. On the other hand, the P3 points for different LF curves show a high spatial variance of the cold air temperature. The maximum temperature is observed in rack R3 since it is located at the farthest distance from both the IRC units, resulting in a higher flow path resistance, as shown by the FNR (see Figure 2). Therefore, the largest pressure drop is experienced by this rack, leading to an increased probability of hot air recirculation from the hot chamber to the cold chamber via the air-blocking brushes.
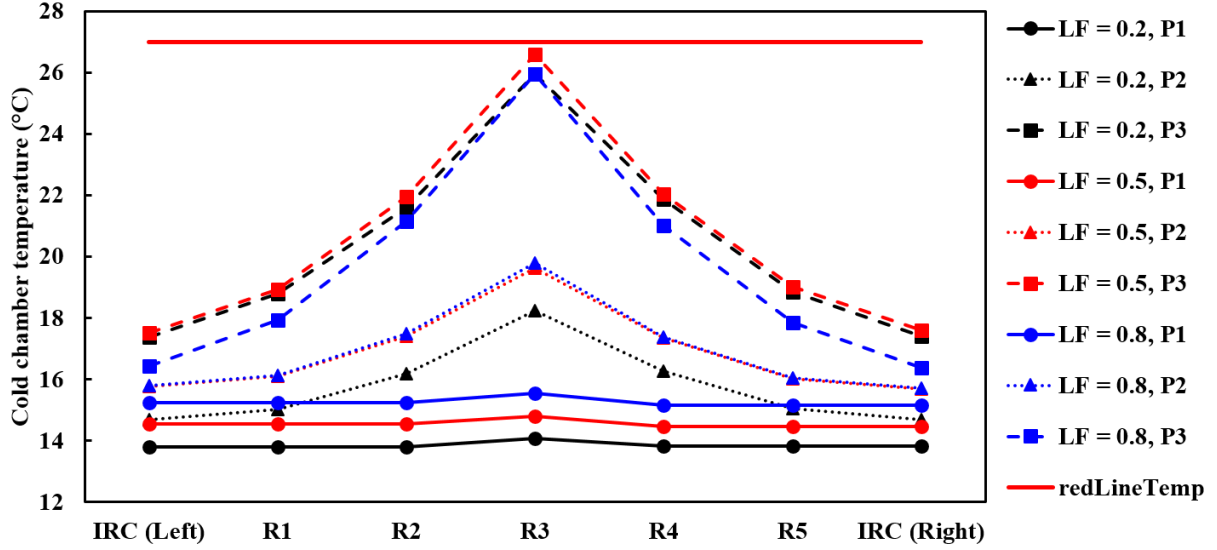
Figure 7: Rack height averaged cold chamber temperature distributions for the nine salient points marked on the Pareto optimal fronts presented in Figure 5. The "redLineTemp" corresponds to the 27 °C maximum allowable cold air temperature for servers. This figure is to be interpreted in accordance with Table 10 and Figure 6.

3.5. *CPR* improvement strategy for large-scale DCs

Upon examining the Pareto fronts presented in Figure 5, it is evident that desired values of η_{ex} and COP_c are obtained by appropriately selecting the cooling parameters $T_{c,w}$ and $\dot{Q}_a$, reducing operational energy expenditure by maximizing COP_c and enhancing effective cooling capacity by maximizing η_{ex}. However, at a higher DC workload (i.e., larger *LF*), there is up to 7.5% degradation in CPR_m due to elevated CPU temperatures. Using an exhaustive search, we found that this degradation could not be avoided. Therefore, further effort is required to improve CPR_m for large-scale DCs which, in turn, will improve $\eta_{c,a}$. Fitting CPR_m with respect to *LF* (Figure 4a), results in the following relation,

$$CPR_m = -0.075(LF) + 0.697,$$
(28)

which is valid for the range $0 < LF \leq 1$.

46

Next, we assume a large-scale DC infrastructure with a total number of IT racks $N_{total} = 100$ that can be constructed by several identical modular blocks of enclosures or "DC pods." Each pod consists of (1) five air-cooled DC racks with a standalone enclosure, (2) two IRC units, (3) a water circulation pump, (4) a VCR chiller, and (5) a pod workload/cooling manager (see Figure 8).
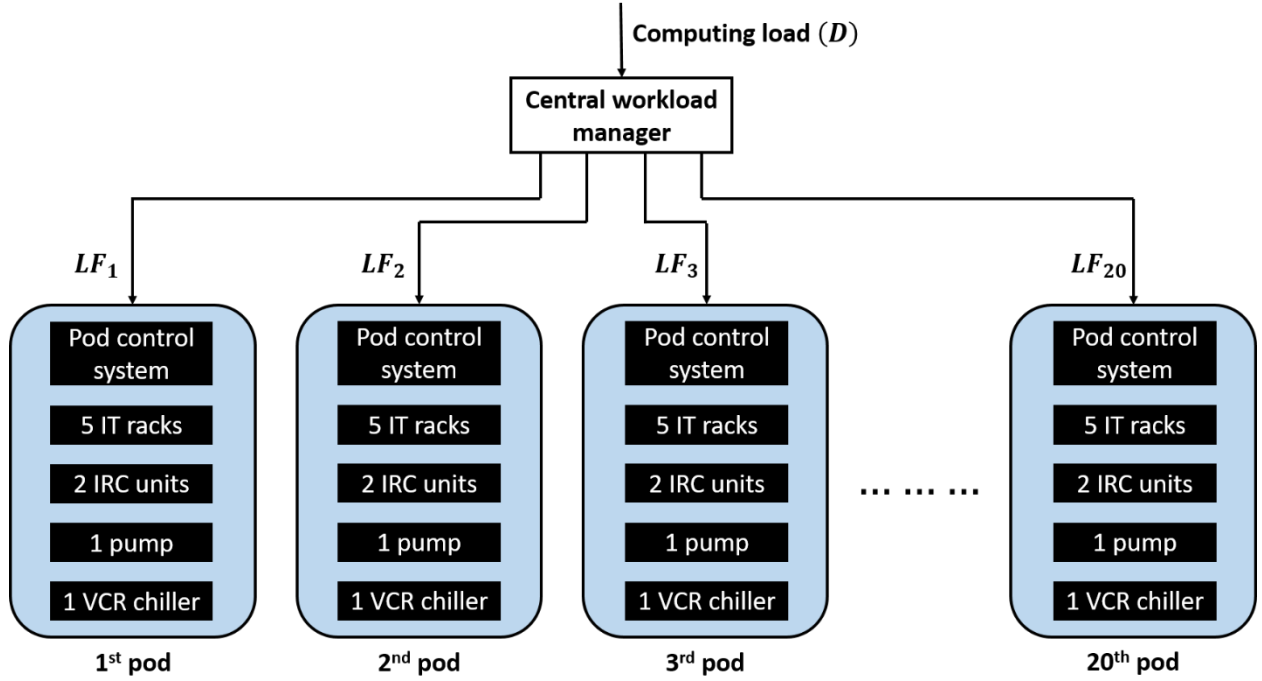

Figure 8: Illustration of the pod management strategy for the 100-rack DC considered. The components inside all the pods are identical and are detailed in Figure 1a. All pods are connected to a central load management system that presets the *LF* for each pod.

Consequently, a 100-rack DC infrastructure requires 20 such pods, i.e., $N_p = \frac{N_{total}}{N_r} = 20$. The maximum achievable computing load for this DC $D^{max} = N_p \times N_r \times N_z \times N_s \times u^{max} = 20 \times 5 \times 5 \times 3 \times 1 = 1500$. We consider scenarios with homogeneous and heterogeneous *LF*s and distribute the IT load $0 < D \leq 1500$ across the DC pods to determine the influence on CPR_m.

Table 11: Results from the heterogeneous *vs.* homogeneous LF assignment across DC pods to improve CPR_m.

Computing load (D)	Strategy 1 (Heterogeneous LF)	CPR_m^{ht}	Strategy 2 (Homogenous LF)	CPR_m^{hm}	Relative improvement $\left(\dfrac{CPR_m^{hm} - CPR_m^{ht}}{CPR_m^{ht}}\right) \times 100$
75	LF=1 (1 pod) LF=0 (19 pods)	0.621	LF=0.05 (20 pods)	0.693	11.6%
150	LF=1 (2 pods) LF=0 (18 pods)	0.621	LF=0.1 (20 pods)	0.689	11.0%
300	LF=1 (4 pods) LF=0 (16 pods)	0.621	LF=0.2 (20 pods)	0.682	9.7%
450	LF=1 (6 pods) LF=0 (14 pods)	0.621	LF=0.3 (20 pods)	0.674	8.5%
600	LF=1 (8 pods) LF=0 (12 pods)	0.621	LF=0.4 (20 pods)	0.667	7.3%
750	LF=1 (10 pods) LF=0 (10 pods)	0.621	LF=0.5 (20 pods)	0.659	6.1%
900	LF=1 (12 pods) LF=0 (8 pods)	0.621	LF=0.6 (20 pods)	0.652	4.9%
1050	LF=1 (14 pods) LF=0 (6 pods)	0.621	LF=0.7 (20 pods)	0.644	3.6%
1200	LF=1 (16 pods) LF=0 (4 pods)	0.621	LF=0.8 (20 pods)	0.637	2.4%
1350	LF=1 (18 pods) LF=0 (2 pods)	0.621	LF=0.9 (20 pods)	0.629	1.2%
1500	LF=1 (20 pods) LF=0 (0 pods)	0.621	LF=1 (20 pods)	0.622	0%

The results presented in Table 11 reveal that homogeneous LF assignment by the central load manager provides up to 11% relative improvement in CPR_m. The heterogeneous LF management scheme (Strategy 1) only considers $LF = 1$ or 0 for the pods. Pods with $LF = 0$ do not contribute to computing demand and therefore CPR_m is not a valid metric for them. In contrast, pods with $LF = 1$ utilize the entire computing capacity of the pod, resulting in poor CPR_m. As the value of

$D \to D^{max}$, the relative enhancement in CPR_m using homogeneous LF management diminishes to 0%.

4. Conclusion

We have developed an advanced methodology to fulfill multiple objectives determining two-dimensional workload distributions and cooling cycle parameters in a five-rack DC equipped with two IRC units. The methodology combines a high-fidelity, spatiotemporal zonal temperature prediction model while quantifying (1) energy, (2) exergy, and (3) computing efficiencies. Several single- and multi-objective problems are solved, addressing three different objectives leading to joint workload and cooling management in a multi-rack DC. The approach reveals non-trivial trade-offs between cooling cycle efficiencies (energy and exergy) and computing efficiency for a wide range of LF. In contrast to prior investigations that only consider the cooling cycle efficiency for single-rack DCs [1, 21], the present work offers additional benefits by quantifying the degradation (or augmentation) of computing efficiency (measured as in GFLOPs per Watt) for a multi-rack DC. Salient findings include:

1. The cooling energy minimization problem populates workload close to the IRC units in a heterogeneous manner and uses a high chilled water temperature $T_{c,w} = 20$ °C.

2. Increasing the LF from 0.2 to 0.8 improves the energy-based metric COP_c up to 12.5% and offers significant energy savings.

3. Trade-offs are observed across COP_c vs. η_{ex} and COP_c vs. CPR_m, where the desired values for all three objectives cannot be obtained by similar values of cooling parameters and workload distribution.

4. The η_{ex} and CPR_m maximization strategy distributes the workload across all of the racks, whereas, the COP_c mediation problem assigns workload close to the IRC units.

5. The metric CPR_m is a weak function of the cooling cycle parameters $T_{c,w}$ and $\dot{Q}_a$. It is predominantly regulated by altering the *LF* of the DC. Increasing the *LF* from 0.2 to 0.8 degrades the CPR_m by up to 7.5% resulting in a lower value of GFLOPs at a higher energy expenditure.

6. The three-dimensional Pareto fronts and corresponding decision variables help to determine detrimental effects on different objectives.

7. An extended approach to manage *LF* in a large-scale DC is presented to improve the overall CPR_m.

The thermally aware, multi-objective workload management scheme for the five-rack, air-cooled DC reveals essential physical insights and opens avenues for future research in joint thermal and workload management for multi-rack DCs. The above methodology is suitable for offline applications in the DC industry, such as investigating the influence of equipment changes and testing what if scenarios. For implementation in real-time DC workload and thermal management, a data-driven methodology using a fully connected feedforward multi-layer perceptron (MLP) neural network can be utilized to capture the interplay between Pareto optimal solutions and corresponding decision variables. Given the inputs (1) $u_{i,j}^z$, (2) $T_{c,w}$, (3) $\dot{Q}_a$, and (4) *LF*, the MLP would be able to predict optimal solutions for (1) COP_c, (2) η_{ex}, and (3) CPR_m within a few seconds.

5. Acknowledgment

6. Appendix 1: Pressure-flow calculation strategy using the flow network model

The airflow inside a DC enclosure with IRC units is pressure-driven and can be modeled using a flow resistance representation (see Figure 2). Our previous experiments demonstrate that the pressure-flow relationship is linear [22]. Hence, the flow resistance is expressed as $R = \Delta P / \dot{Q}$, where ΔP and $\dot{Q}$ are the characteristic pressure drop and flowrate, respectively. The experimentally determined values for different resistances R_H^f, R_V^f, R_H^b, R_V^b, and R_{br} are available in [22]. Different flow interactions of a zone with its neighboring zones are, (1) right $\dot{Q}_{(i+1,j) \to (i,j)}$, (2) left $\dot{Q}_{(i-1,j) \to (i,j)}$, (3) top $\dot{Q}_{(i,j+1) \to (i,j)}$, (4) bottom $\dot{Q}_{(i,j-1) \to (i,j)}$, (5) leakage flow between front and back chambers through brushes, i.e., $\dot{Q}_{i,j}^{b \to f}$ or $\dot{Q}_{i,j}^{f \to b}$, and (6) flow induced by server fans $\dot{Q}_{i,j}^z$. A schematic of these neighboring flow resistances and pressures is provided in Figure A1 for a single server zone.
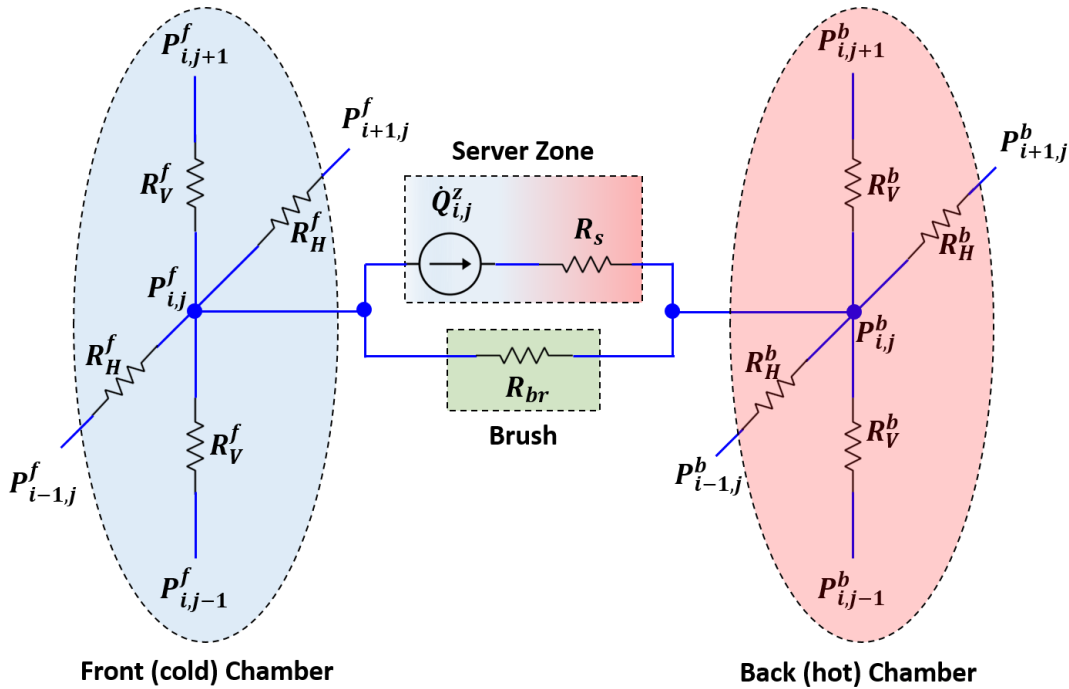

Figure A1: Schematic of neighboring flow resistances and pressures for a single server zone. The flow across a resistance depends on the magnitude and sign of the pressure difference. A

combination of several such server zones and the IRC units results in the generalized flow network representation shown in Figure 2.

Subsequently, the zonal flowrate balance in the front chamber for an active or idle server [21, 22],

$$\dot{Q}^f_{(i+1,j)\to(i,j)} + \dot{Q}^f_{(i-1,j)\to(i,j)} + \dot{Q}^f_{(i,j+1)\to(i,j)} + \dot{Q}^f_{(i,j-1)\to(i,j)} + \dot{Q}^{b\to f}_{i,j} - \dot{Q}^z_{i,j} = 0, \tag{A1}$$

$$\Rightarrow \frac{P^f_{i+1,j}-P^f_{i,j}}{R^f_H} + \frac{P^f_{i-1,j}-P^f_{i,j}}{R^f_H} + \frac{P^f_{i,j+1}-P^f_{i,j}}{R^f_V} + \frac{P^f_{i,j-1}-P^f_{i,j}}{R^f_V} + \frac{P^b_{i,j}-P^f_{i,j}}{R_{br}} - \dot{Q}^z_{i,j} = 0, \tag{A2}$$

$$\Rightarrow \alpha^f\left[P^f_{i+1,j} + P^f_{i-1,j}\right] + \beta^f\left[P^f_{i,j+1} + P^f_{i,j-1}\right] + \gamma P^b_{i,j} - (2\alpha^f + 2\beta^f + \gamma)P^f_{i,j} - \dot{Q}^z_{i,j} = 0. \tag{A3}$$

While that in the back chamber is expressed as,

$$\dot{Q}^b_{(i+1,j)\to(i,j)} + \dot{Q}^b_{(i-1,j)\to(i,j)} + \dot{Q}^b_{(i,j+1)\to(i,j)} + \dot{Q}^b_{(i,j-1)\to(i,j)} + \dot{Q}^{f\to b}_{i,j} + \dot{Q}^z_{i,j} = 0, \tag{A4}$$

$$\Rightarrow \frac{P^b_{i+1,j}-P^b_{i,j}}{R^f_H} + \frac{P^b_{i-1,j}-P^b_{i,j}}{R^f_H} + \frac{P^b_{i,j+1}-P^b_{i,j}}{R^f_V} + \frac{P^b_{i,j-1}-P^b_{i,j}}{R^f_V} + \frac{P^b_{i,j}-P^f_{i,j}}{R_{br}} + \dot{Q}^z_{i,j} = 0, \tag{A5}$$

$$\Rightarrow \alpha^b\left[P^b_{i+1,j} + P^b_{i-1,j}\right] + \beta^b\left[P^b_{i,j+1} + P^b_{i,j-1}\right] + \gamma P^f_{i,j} - (2\alpha^b + 2\beta^b + \gamma)P^b_{i,j} + \dot{Q}^z_{i,j} = 0. \tag{A6}$$

Likewise, the flowrate balance for the zones in the front chamber adjacent to the IRC units yields,

$$\dot{Q}^f_{(i+1,j)\to(i,j)} - \frac{\dot{Q}_a}{N_z N_{cu}} = 0, \tag{A7}$$

$$\Rightarrow \frac{P^f_{i+1,j}-P^f_{i,j}}{R^f_H} - \frac{\dot{Q}_a}{N_z N_{cu}} = 0, \tag{A8}$$

$$\Rightarrow \alpha^f\left[P^f_{i+1,j} - P^f_{i,j}\right] - \frac{\dot{Q}_a}{N_z N_{cu}} = 0, \tag{A9}$$

and that in the back chamber is expressed as,

$$\dot{Q}^b_{(i+1,j)\to(i,j)} + \frac{\dot{Q}_a}{N_z N_{cu}} = 0, \tag{A10}$$

$$\Rightarrow \frac{P^b_{i+1,j}-P^b_{i,j}}{R^f_H} + \frac{\dot{Q}_a}{N_z N_{cu}} = 0, \tag{A11}$$

$$\Rightarrow \alpha^b\left[P^b_{i+1,j} - P^b_{i,j}\right] + \frac{\dot{Q}_a}{N_z N_{cu}} = 0. \tag{A12}$$

Equations (A3), (A6), (A9), and (A12) are final forms of the pressure-flow calculation, representing two sets of linear equations. The first results in a two-dimensional pressure matrix in the front chamber $\left[P_{i,j}^{f}\right]$, while the latter provides a pressure matrix in the back chamber $\left[P_{i,j}^{b}\right]$. The pressure variation across the geometry is influenced by the following factors.

- The distance between the IRC units and different racks offers a resistance, decreasing the cold air delivered to the racks at farther distances.

- A mismatch between the total air suction of servers and supply by the IRC units creates a pressure difference between the front and back chambers (~10 Pa) [30, 39]. According to the sign of the pressure difference, this produces a net leakage flow through the brushes across the two chambers.

- The combined effect of these two influences creates a larger pressure difference between front and back chamber zones which lie farthest from IRC units (R3 in this case).

7. References

[1]   S. MirhoseiniNejad, H. Moazamigoodarzi, G. Badawy, and D. G. Down, "Joint data center cooling and workload management: A thermal-aware approach," *Future Generation Computer Systems,* vol. 104, pp. 174-186, 2020.
[2]   S. MirhoseiniNejad, G. Badawy, and D. G. Down, "Holistic thermal-aware workload management and infrastructure control for heterogeneous data centers using machine learning," *Future Generation Computer Systems,* vol. 118, pp. 208-218, 2021.
[3]   B. Shi and A. Srivastava, "Unified datacenter power management considering on-chip and air temperature constraints," *Sustainable Computing: Informatics and Systems,* vol. 1, pp. 91-98, 2011.
[4]   S. K. Garg, S. K. Gopalaiyengar, and R. Buyya, "SLA-based resource provisioning for heterogeneous workloads in a virtualized cloud datacenter," in *International conference on Algorithms and architectures for parallel processing*, 2011, pp. 371-384.
[5]   S. Ghorbani, Z. Yang, P. B. Godfrey, Y. Ganjali, and A. Firoozshahian, "Drill: Micro load balancing for low-latency data center networks," in *Proceedings of the Conference of the ACM Special Interest Group on Data Communication*, 2017, pp. 225-238.
[6]   R. Gupta, S. Asgari, H. Moazamigoodarzi, S. Pal, and I. K. Puri, "Cooling architecture selection for air-cooled Data Centers by minimizing exergy destruction," *Energy,* p. 117625, 2020.
[7]   H. Moazamigoodarzi, P. J. Tsai, S. Pal, S. Ghosh, and I. K. Puri, "Influence of cooling architecture on data center power consumption," *Energy,* vol. 183, pp. 525-535, 2019.
[8]   K. Ebrahimi, G. F. Jones, and A. S. Fleischer, "A review of data center cooling technology, operating conditions and the corresponding low-grade waste heat recovery opportunities," *Renewable and Sustainable Energy Reviews,* vol. 31, pp. 622-638, 2014.

[9]   Z. Ding, Y. Cao, L. Xie, Y. Lu, and P. Wang, "Integrated stochastic energy management for data center microgrid considering waste heat recovery," *IEEE Transactions on Industry Applications,* vol. 55, pp. 2198-2207, 2019.

[10]   P. Huang, B. Copertaro, X. Zhang, J. Shen, I. Löfgren, M. Rönnelid*, et al.*, "A review of data centers as prosumers in district energy systems: Renewable energy integration and waste heat reuse for district heating," *Applied Energy,* vol. 258, p. 114109, 2020.

[11]   Y. Bai, L. Gu, and X. Qi, "Comparative study of energy performance between chip and inlet temperature-aware workload allocation in air-cooled data center," *Energies,* vol. 11, p. 669, 2018.

[12]   Q. Tang, S. K. Gupta, and G. Varsamopoulos, "Thermal-aware task scheduling for data centers through minimizing heat recirculation," in *2007 IEEE International Conference on Cluster Computing*, 2007, pp. 129-138.

[13]   J. D. Moore, J. S. Chase, P. Ranganathan, and R. K. Sharma, "Making Scheduling" Cool": Temperature-Aware Workload Placement in Data Centers," in *USENIX annual technical conference, General Track*, 2005, pp. 61-75.

[14]   R. K. Sharma, C. E. Bash, C. D. Patel, R. J. Friedrich, and J. S. Chase, "Balance of power: Dynamic thermal management for internet data centers," *IEEE Internet Computing,* vol. 9, pp. 42-49, 2005.

[15]   M. T. Chaudhry, T. Ling, S. A. Hussain, and A. Manzoor, "Minimizing thermal stress for data center servers through thermal-aware relocation," *The Scientific World Journal,* vol. 2014, 2014.

[16]   L. Silva-Llanca, A. Ortega, K. Fouladi, M. del Valle, and V. Sundaralingam, "Determining wasted energy in the airside of a perimeter-cooled data center via direct computation of the Exergy Destruction," *Applied Energy,* vol. 213, pp. 235-246, 2018.

[17]   A. Bhalerao, K. Fouladi, L. Silva-Llanca, and A. P. Wemhoff, "Rapid prediction of exergy destruction in data centers due to airflow mixing," *Numerical Heat Transfer, Part A: Applications,* vol. 70, pp. 48-63, 2016.

[18]   A. J. Shah, V. P. Carey, C. E. Bash, and C. D. Patel, "Exergy analysis of data center thermal management systems," *Journal of Heat Transfer,* vol. 130, 2008.

[19]   A. J. Díaz, R. Cáceres, J. M. Cardemil, and L. Silva-Llanca, "Energy and exergy assessment in a perimeter cooled data center: The value of second law efficiency," *Applied Thermal Engineering,* vol. 124, pp. 820-830, 2017.

[20]   K. Fouladi, A. P. Wemhoff, L. Silva-Llanca, K. Abbasi, and A. Ortega, "Optimization of data center cooling efficiency using reduced order flow modeling within a flow network modeling approach," *Applied Thermal Engineering,* vol. 124, pp. 929-939, 2017.

[21]   R. Gupta, H. Moazamigoodarzi, S. MirhoseiniNejad, D. G. Down, and I. K. Puri, "Workload management for air-cooled data centers: An energy and exergy based approach," *Energy,* vol. 209, p. 118485, 2020.

[22]   H. Moazamigoodarzi, R. Gupta, S. Pal, P. J. Tsai, S. Ghosh, and I. K. Puri, "Modeling temperature distribution and power consumption in IT server enclosures with row-based cooling architectures," *Applied Energy,* vol. 261, p. 114355, 2020.

[23]   S. J. Ovaska, R. E. Dragseth, and S. A. Hanssen, "Direct-to-chip liquid cooling for reducing power consumption in a subarctic supercomputer centre," *International Journal of High Performance Computing and Networking,* vol. 9, pp. 242-249, 2016.

[24]   A. A. Moskovsky, E. A. Druzhinin, A. B. Shmelev, V. V. Mironov, and A. Semin, "Server Level Liquid Cooling: Do Higher System Temperatures Improve Energy Efficiency?," *Supercomputing frontiers and innovations,* vol. 3, pp. 67-74, 2016.

[25]   D. C. Price, M. A. Clark, B. R. Barsdell, R. Babich, and L. J. Greenhill, "Optimizing performance-per-watt on GPUs in high performance computing," *Computer Science-Research and Development,* vol. 31, pp. 185-193, 2016.

[26]   J. Shin and E. Seo, "Impact of Data Center Cooling Technology to Effectiveness of Turbo-Mode," in *2020 International Conference on Information and Communication Technology Convergence (ICTC)*, 2020, pp. 1691-1693.

[27]   S. Mirhoseininejad, G. Badawy, and D. G. Down, "A Data-driven, Multi-setpoint Model Predictive Thermal Control System for Data Centers," *Journal of Network and Systems Management,* vol. 29, pp. 1-22, 2020.

[28]   S. Asgari, H. Moazamigoodarzi, P. J. Tsai, S. Pal, R. Zheng, G. Badawy*, et al.*, "Hybrid surrogate model for online temperature and pressure predictions in data centers," *Future Generation Computer Systems,* vol. 114, pp. 531-547, 2021.

[29]   S. Asgari, S. MirhoseiniNejad, H. Moazamigoodarzi, R. Gupta, R. Zheng, and I. K. Puri, "A Gray-Box Model for Real-Time Transient Temperature Predictions in Data Centers," *Applied Thermal Engineering,* p. 116319, 2020/11/13/ 2020.

[30]   H. Moazamigoodarzi, S. Pal, S. Ghosh, and I. K. Puri, "Real-time temperature predictions in it server enclosures," *International Journal of Heat and Mass Transfer,* vol. 127, pp. 890-900, 2018.

[31]   Y. Li, X. Wang, P. Luo, and Q. Pan, "Thermal-aware hybrid workload management in a green datacenter towards renewable energy utilization," *Energies,* vol. 12, p. 1494, 2019.

[32]   Z. Abbasi, G. Varsamopoulos, and S. K. Gupta, "Tacoma: Server and workload management in internet data centers considering cooling-computing power trade-off and energy proportionality," *ACM Transactions on Architecture and Code Optimization (TACO),* vol. 9, pp. 1-37, 2012.

[33]   L. Wang, S. U. Khan, and J. Dayal, "Thermal aware workload placement with task-temperature profiles in a data center," *The Journal of Supercomputing,* vol. 61, pp. 780-803, 2012.

[34]   X. Li, P. Garraghan, X. Jiang, Z. Wu, and J. Xu, "Holistic virtual machine scheduling in cloud datacenters towards minimizing total energy," *IEEE Transactions on Parallel and Distributed Systems,* vol. 29, pp. 1317-1331, 2017.

[35]   Q. Fang, J. Wang, Q. Gong, and M. Song, "Thermal-aware energy management of an HPC data center via two-time-scale control," *IEEE Transactions on Industrial Informatics,* vol. 13, pp. 2260-2269, 2017.

[36]   Z. Liu, Y. Chen, C. Bash, A. Wierman, D. Gmach, Z. Wang*, et al.*, "Renewable and cooling aware workload management for sustainable data centers," in *Proceedings of the 12th ACM SIGMETRICS/PERFORMANCE joint international conference on Measurement and Modeling of Computer Systems*, 2012, pp. 175-186.

[37]   R. G. Co., "TopTherm LCP Inline flush CW, Assembly and operating instructions," ed, 2015, pp. 1-92.

[38]   TRANE, "Air-cooled liquid chillers, 10 to 60 Tons," in *Product catalog*, ed, 2004, pp. 1-52.

[39]   H. Moazamigoodarzi, S. Pal, D. Down, M. Esmalifalak, and I. K. Puri, "Performance of a rack mountable cooling unit in an IT server enclosure," *Thermal Science and Engineering Progress,* vol. 17, p. 100395, 2020.

[40]   J. W. VanGilder, Z. Pardey, C. Healey, and X. Zhang, "A compact server model for transient data center simulations," *ASHRAE Transactions,* vol. 119, pp. 358-370, 2013.

[41]   C. Jin, X. Bai, C. Yang, W. Mao, and X. Xu, "A review of power consumption models of servers in data centers," *Applied Energy,* vol. 265, p. 114806, 2020.

[42]   S.-W. Ham, M.-H. Kim, B.-N. Choi, and J.-W. Jeong, "Simplified server model to simulate data center cooling energy consumption," *Energy and Buildings,* vol. 86, pp. 328-339, 2015.

[43]   H. Packard, "Quickspecs: HP ProLiant DL360 Generation 5 (G5)," in *Product datasheet*, ed, 2007, pp. 1-43.

[44]   J. M. Gordon, K. Ng, and H. Chua, "Optimizing chiller operation based on finite-time thermodynamics: universal modeling and experimental confirmation," *International Journal of Refrigeration,* vol. 20, pp. 191-200, 1997.

[45]   S. M. M. Nejad, G. Badawy, and D. G. Down, "Eawa: Energy-aware workload assignment in data centers," in *2018 International Conference on High Performance Computing & Simulation (HPCS)*, 2018, pp. 260-267.

[46]   R. Steinbrecher and R. Schmidt, "Data center environments," *ASHRAE J,* vol. 42, p. e49, 2011.